The Thesis Committee for Joe Wayne Skeens
Certifies that this is the approved version of the following Thesis:

On the Crushing Behavior and Microstructure of Closed-Cell Polymeric Foams: Experiments and Phenomenological Investigation

APPROVED BY
SUPERVISING COMMITTEE:

Stelios Kyriakides, Supervisor

Kenneth Liechti

On the Crushing Behavior and Microstructure of Closed-Cell Polymeric Foams: Experiments and Phenomenological Investigation

by

Joe Wayne Skeens

Thesis

Presented to the Faculty of the Graduate School of

The University of Texas at Austin

in Partial Fulfillment

of the Requirements

for the Degree of

Master of Science in Engineering

The University of Texas at Austin

December 2023

Acknowledgements

I am very grateful to Dr. Stelios Kyriakides for the continuous guidance and support he offered throughout the work conducted for this thesis. Thanks to Joe Pokluda for his machining work that enabled much of the experimental setup. Thanks also to Scott Messec for providing and supporting the computing resources to do the image analysis. Special thanks to Rasesh Kapadia for his help in scanning the foam specimens at higher resolution. I acknowledge with thanks the University of Texas at Austin for supporting this work through a Cockrell School of Engineering Fellowship and through teaching assistantships. I am also grateful to Diab Americas LP, Dallas, TX for supplying the Divinycell foam used in this work. Finally, I am indebted to my fellow graduate student Solon Tsimpoukis for his repeated help in setting up and carrying out the foam crushing experiments.

Abstract

On the Crushing Behavior and Microstructure of Closed-Cell Polymeric Foams: Experiments and Phenomenological Investigation

Joe Wayne Skeens, M.S.E.

The University of Texas at Austin, 2023

Supervisor: Stelios Kyriakides

This thesis investigates the compressive behavior and crushing of Divinycell H100 under combined axial compression and external pressure. Divinycell H100 is a closed-cell polymeric foam with a relative density of 0.077 that is used extensively in sandwich composites for marine, transportation, energy, and infrastructure applications. The study starts with characterization of the microstructure using micro-computed tomography. It has a nearly monodisperse polyhedral microstructure with mean cell size and wall thickness of 0.50 mm and 0.0348 mm respectively. A custom triaxial apparatus is used to compress cylindrical specimens at different levels of external pressure. A typical axial stress-displacement response exhibits a stiff elastic branch that terminates into a maximum beyond which deformation localizes into a horizontal axisymmetric, radially contracted band of crushed cells. The band then propagates axially with the stress remaining essentially constant. Both the initial stress maximum and the plateau stress

decrease linearly as the pressure increases. X-ray imaging of the microstructure of a specimen crushed axially at zero pressure confirmed that during the stress plateau, a highly crushed zone of cells with an average strain of about 50% coexists with zones of essentially undeformed cells. Postmortem images of specimens tested under triaxial loading reveal a similar evolution of crushing. Above a critical pressure, the mode of instability switches to predominantly lateral contraction that evolves into a neck. This is also the mechanism of failure under pure pressure. The localized crushing behavior observed is similar to that of low-density open-cell foams and the results should inform and guide further development of homogenized models for this class of materials.

Table of Contents

Chapter 1: Introduction

Closed-cell polymeric foams consist of randomly packed polyhedral cells with thin membranes covering their polygonal faces generated by a foaming process. The microstructure bestows excellent stiffness- and strength-to-weight ratios making the stiffer/stronger foams, referred to as "rigid," widely used as cores in sandwich construction. Rigid foams, often sandwiched between lightweight composite faceplates, are used in marine, aerospace, and automotive applications, in wind-turbine blades, and in other structures. Under compression, the slender cellular microstructure buckles and collapses at relatively low stress, inducing strain levels on the order of 70%. These outstanding energy absorption characteristics make foams one of the most widely used classes of materials in impact and shock mitigation applications including as bumpers in vehicles, in helmets, packaging, and many others (e.g., Gibson and Ashby, 1997; Ashby et al., 2000; Gibson et al., 2010; Tomin and Kmetty, 2022). Such foams are also used in noise abatement and thermal insulation.

1.1 Investigation of Polymeric Foams in Literature

A major objective of the research community is to relate the microstructure and base material properties of foams to their unique energy absorption and deformation mechanisms. Gibson and Ashby's (1997) pioneering book paved the way by using simple models to demonstrate such connections for natural and manmade cellular materials (see also, Gibson et al., 2010). It has been followed by increasingly more advanced phenomenological models (e.g., Deshpande and Fleck, 2000, 2001; Zhu et al., 2019;

Yang and Kyriakides, 2020a) and micromechanically accurate (e.g., Gong et al., 2005; Jang et al., 2008; Gaitanaros et al., 2012; Gaitanaros and Kyriakides, 2014; Zheng et al., 2014; Chen et al., 2015; Jang et al., 2015; Pascalis et al., 2016; Beckmann and Hohe, 2016; Su and Jang, 2018, 2022; Zhou, 2023) analytical and numerical models that constitute today's vast literature on cellular materials. The field has been further broadened by the related architected periodic cellular materials (e.g., Schaedler and Carter, 2016; Greer and Deshpande, 2019) brought about by the advent of 3-D printing and additive manufacturing.

The present study is focused on the compressive behavior of Divinycell H100, a "rigid," closed-cell polymeric foam (Divinycell H, 2022). Because of its wide use in engineering applications, this family of foam has received significant attention in the scientific literature regarding its elastic properties, strength, energy absorption, dynamic behavior, etc. (e.g., Steeves and Fleck, 2004; Liu et al., 2020; Tang et al., 2022; Rahimidehgolan and Altenhof, 2023).

Early work in the deformation of cellular materials was carried out by Shaw and Sata (1966), who conducted experiments with polystyrene foam and proposed a cellular collapse mechanism governing the uniaxial compressive deformation. The authors additionally found that the uniaxial yield criterion is the maximum compressive stress. Gibson et al. (1989) and Triantafillou et al. (1989) further modeled the multi-axial yield behavior of cellular materials and conducted tests of these yield criteria on open- and closed-cell foams, both flexible and rigid. The study concluded that the failure surface under compression of the closed-cell, rigid polyurethane foam traces an ellipsoid in the principal stress space.

Deshpande and Fleck (2001) investigated the behavior of the Divinycell H100 and H200 foams and used combinations of axial and radial tension and compression

results to fit a yield surface describing an ellipse in the space of mean stress and von Mises effective stress, capped by a maximum compressive principal stress criterion.

Shafiq et al. (2015) examined the multi-axial yield of Divinycell H100 foams with a custom-built triaxial testing apparatus designed to simultaneously crush a foam specimen along three independent axes. The authors collected extensive tension and compression data in uniaxial, biaxial, and triaxial loading, and used this data to develop an energy-based yield surface with an additional linear pressure dependence. Yang and Kyriakides (2020a) used numerical true triaxial data from Yang and Kyriakides (2019) to develop a continuum model of the deformation of an open-celled foam accounting for the inhomogeneous crushing behavior associated with the localized propagation of crushing.

Major research efforts have also been made to model the microstructure of open- and closed-cell foams. In particular, X-ray tomography has emerged as a powerful technique to non-destructively probe the microstructure and its evolution under loading of cellular materials. Salvo et al. (2003) used X-ray tomography to probe the evolution of the structure of an ALPORAS open-celled aluminum foam before and during compression, analyzing the reconstructed images to comment on the microstructural deformation mechanisms. Daphalapurkar et al. (2008) use micro-computed X-ray tomography to conduct in-situ observations of a closed-cell polymer foam undergoing compression, using the reconstructed images to identify specific locations of bending and buckling of cell-walls that compress into a “shear band” as deformation continues. The authors used the collected fine-scale stress and strain data to construct and solve an inverse problem relating the deformation to the material properties of the foam. Jang and Kyriakides (2009) used X-ray tomography to monitor the evolution of crushing bands through an open-cell aluminum alloy foam. They concluded that compression causes ligament buckling in a weaker zone that leads to the collapse of bands of cells. Local

deformation is arrested when the cell ligaments come into contact. The crushing continues at neighboring rows of cells that have been destabilized. This continues at nearly constant stress until the whole specimen is crushed, when the response of the densified material begins rising again. This behavior placed the problem in the class of propagating instabilities.

More recently, Chai et al. (2020) used X-ray micro-computed tomography to investigate the microstructural properties of a polymethacrylide closed-cell foam, identifying individual cell boundaries and fitting a distribution of cell size. During axial compression, the authors used in-situ tomography to identify 3-D local strain values throughout the foam specimen. Tomographic data were used to produce a finite element model and investigate the buckling mechanisms of cell walls. Su and Jang (2022) utilized micro-computed tomography in conjunction with image processing algorithms to measure the geometric characteristics of an ALPORAS closed-cell aluminum foam including cell size, surface area, cell shape, and aspect ratio. The detailed cell geometry was used to produce a high-fidelity numerical foam model from Laguerre tessellation that was tested in finite element simulations.

1.2 Scope of this Study

This manuscript presents the results of an investigation on the compressive behavior and crushing of a Divinycell H100 closed-cell foam under triaxial loads. Chapter 2 starts with an analysis of the cellular microstructure using X-ray tomography. Cell size, anisotropy, and face thickness are investigated using this tomographic data. A simple Kelvin cell model is developed to relate the cell face thickness to the concentration of the foam in the nodes for a measured relative density. While X-ray

tomography has previously been used to successfully capture the geometric characteristics of microstructures, the use of tomography to monitor the evolution of deformation during crushing of closed-cell foams is very limited. Furthermore, these efforts have been confined to specimen sizes a few cells (~5) in width and height. One of the objectives of the present work was to capture the evolution of crushing in D-H100 closed-cell foams for specimens with a much larger number of cells in order to provide more definitive and reliable information and data to future modeling efforts.

The main thrust of the investigation is the use of a custom triaxial test apparatus to conduct compression experiments on D-H100 foam specimens at different pressure levels. Chapter 3 describes the triaxial test apparatus that was developed for this purpose. The design loads and materials used in the apparatus are discussed at length, and the custom-designed internal load cell used within the test apparatus is detailed. A description is also provided of the assembly of the load cell and the setup of the crushing experiments.

Chapter 4 describes the set of triaxial experiments that were performed. The results from 11 compression experiments are used to fit a Drucker-Prager compressible yield surface (Drucker and Prager, 1952) for the material. At higher pressure levels, a distinct deformation behavior dominates that is characterized by radial contraction rather than steady state axial propagation of banded crushing zones. Results from a special experiment in which the evolution of crushing is monitored by X-ray tomography at various points of deformation using a custom holding device are used to demonstrate that this behavior belongs in the class of propagating instabilities. These reconstructed images

show the formation and propagation of a localized crushing zone that coexists with regions of mostly undeformed cells. Chapter 5 summarizes the results and draws some major conclusions.

Chapter 2: Foam Microstructure Characterization

The microstructural properties of the Divinycell H100 closed-cell foam were investigated in detail via a series of X-ray scans in a μCT 80 computed tomography scanner. The scans were performed with a power of 8 W, 45 kVp, 177 μA, a 1 second integration time, and 2 averages per sample. The minimum voxel size of the μCT 80 system is 10 μm. After collecting the 3-D computed tomography data for a foam sample, open-source scientific tools developed for the image analysis package *Fiji* were employed to analyze the foam microstructure.

2.1 Foam Properties and X-Ray Tomography

The foam samples that were analyzed in the μCT 80 system were cylinders 51 mm tall and 38 mm in diameter (2.0× 1.5 in). The samples were milled from a mother plate without modifying the thickness along the rise direction. The data collected from the X-ray scanning machine were stored as TIFF files ranging from 1-10 GB in size. The datasets were scans of the full cylinder diameter of about 2 mm height along the length. This volume captured on the order of 5000–10000 cells.

From the raw TIFF files, images of the microstructure were generated with the *3D Viewer* plugin. Fig. 2.1 shows one such visualization, where image (a) is the transverse plane of the foam sample, and (b) is the rise direction of the sample. This visualization reveals several important facts. First, that material concentrates at the nodes joining four faces, whereas intersections of three faces or edges do not attract as much material. Also,

while the transverse direction cells do not show a preferred direction, in the rise direction, the cells are visibly elongated, demonstrating significant anisotropy. Finally, the faces do not appear to significantly change in thickness along their length.

For quantitative analysis, the data were processed with a series of open-source software packages written as plugins for *Fiji*, an image processing software package based on *ImageJ*, a scientific image analysis product originally developed by the National Institutes of Health (Schindelin et al., 2012).

Fig. 2.2 shows the three steps involved in processing the 3-D microtomography data collected from a foam sample. On the left (a), a single slice of a TIFF image stack is shown from a µCT 80 scan. The middle image (b) shows the same slice after intermediate processing. The low density of the foam makes noise mitigation an important first step. A 3-dimensional Gaussian filter is applied to the data with a kernel size of 1 voxel. A lower threshold of about 10% of the maximum intensity is then applied. These two steps remove noise that typically manifests as speckles in the empty areas of the scan. After thresholding, a 3-D watershed split algorithm is run on the dataset.

This routine computes a Euclidean distance map from cell boundaries, then finds the local maximum of each cell in a 3-D sense as the voxel with the largest distance to the cell boundary, roughly corresponding to the geometric center of the cell. The seeds then grow according to the magnitude of the distance mapped to the center of each cell, and the cell boundaries interact to draw new cell boundaries. The 3-D watershed split routine is necessary because the PVC material in Divinycell H100 foam is of low enough density

that it is difficult to separate from noise in the scan, and thus many cell boundaries are discarded by thresholding in the previous step.

Finally, image (c) shows the cells after identification by the *BoneJ Extended Particle Analyzer* (Doube et al., 2010; Domander et al., 2021). The particle analyzer generates a surface mesh and finds the volume enclosed within, indexed by the location of the center of the cell. The volume identified as a particle is an open region in the microstructure of the foam not including the material of the foam itself. The volume of the cell is related to a characteristic cell size by taking the cell size as the diameter of a sphere with equivalent volume,

$$D = \left(\frac{6V}{\pi} \right)^{\frac{1}{3}}. \tag{2.1}$$

Fig. 2.3 shows a cross-section of 3-D microtomography data with the cells identified by the *Extended Particle Analyzer* highlighted in varying colors. The broken cells on the edge of the foam sample are excluded, with only complete cells shown as identified by the particle analyzer and included in additional quantitative analyses.

2.2 Cell Size, Morphology, and Distribution

The full set of cell sizes in a scanned volume of diameter 38 mm (1.5 in) and height 5 mm (0.2 in) were used to fit a lognormal distribution of cell sizes to the data in a least squares sense. This distribution fitting was performed with the *fit* routine from the SciPy statistics module (Virtanen et al., 2020). Fig. 2.4 shows the fitted lognormal distribution and its mean and standard deviation as well as the binned cell size data to

which the distribution was fitted. The identified mean value, $\bar{D}$, is 0.501 mm with a standard deviation of 0.092 mm.

As a measure of polydispersity, the cell diameter relative deviation,

$$\sum_D = \frac{1}{\bar{D}} \sqrt{\frac{1}{N} \sum_i^N \left(D_i - \bar{D} \right)^2} , \tag{2.2}$$

can also be retrieved from the cell size data. $\sum_D$ is found to be about 0.183 for the foam, where a perfectly monodisperse foam in which all cells have equal volume has a relative diameter deviation $\sum_D = 0$. This indicates a non-negligible but relatively low polydispersity.

The anisotropy of the samples has also been experimentally investigated with the cell characteristics computed by the *BoneJ Extended Particle Analyzer*. As the *Extended Particle Analyzer* identifies contiguous cell volumes, it produces a 3-D dataset in which each voxel that belongs to an identified cell is marked with a common integer cell number. By analyzing the geometry of these contiguous cells, the maximum extents of the cell in $\{x, y, z\}$ were determined, with *z* oriented along the rise direction. The maximum and minimum extents in each direction for each cell were then used to calculate the ratios $\{\lambda_{xy}, \lambda_{xz}, \lambda_{yz}\}$ for example as follows:

$$\lambda_{xz} = \frac{1}{N} \sum_{i=1}^{N} \frac{z_{i\max} - z_{i\min}}{x_{i\max} - x_{i\min}} . \tag{2.3}$$

The evaluated mean values are $\{\bar{\lambda}_{xy}, \bar{\lambda}_{xz}, \bar{\lambda}_{yz}\}$ = {1.0, 1.4, 1.4} with standard deviations of {0.21, 0.29, 0.29}. The distribution of measured cell anisotropies is shown

in Figs. 2.5 and 2.6 in the form of histograms. The anisotropy between the rise and transverse directions is 1.4, and the mode of the distribution is about 1.3. As expected, there is no significant anisotropy in the $x-y$ plane and the measured anisotropy value is 1.0.

The face thicknesses of the Divinycell H100 foam sample were analyzed with a high-resolution scan of a small ($15\times 15\times 1.254$ mm, $0.59\times 0.59\times 0.049$ in) sample at 6 μm resolution provided by Scanco. The thickness was evaluated by the *BoneJ* implementation of the *Local Thickness* (Dougherty and Kunzelmann, 2007) plugin, which calculates the thickness at each data point as the diameter of the largest sphere that fits within the structure and contains the indicated point. The algorithm utilizes a Euclidean distance transformation to produce a distance map from each point of interest to the edge of the structure.

The full 3-D data is collected on a point-by-point basis, where each voxel is assigned a float thickness value. A view of this 3-D thickness data is shown in Fig. 2.7. A lognormal distribution is fit to the histogram of local thicknesses. This distribution of face thickness therefore represents a relative frequency by volume throughout the sample rather than a number density of thickness by ligament or face as is commonly seen in the literature. Nevertheless, the mode of this distribution represents the most common face thickness in the sample as a function of volume, and the distribution of thickness is a useful tool in fitting an empirical face shape function. Fig. 2.8 shows the fitted lognormal distribution and the thickness data as histogram. The mode of the lognormal distribution

is 0.0222 mm with a standard deviation 0.0213 mm. The parameters of the lognormal fits in Fig. 2.4 and 2.8 are available in Table 2.2.

2.3 A Simplified Model of Face Thickness and Relative Density

To relate the face thickness to the relative density of a closed-cell foam assuming that the effect of polydispersity is minimal, a simple repeating tetrakaidecahedron or Kelvin cell model was used to establish a constraint between these two parameters. This analysis makes use of the geometric relationships defined for the Kelvin cell model in Sullivan (2007) (see also Gong et al., 2005).

The dimensions of the regular Kelvin cell are shown in Fig. 2.9. Using a face length L, the height, H, and diameter, D, are given by,

$$H = 4L\sin\theta = 2\sqrt{2}L, \tag{2.2}$$

$$D = 2L\cos\theta + \sqrt{2}L = 2\sqrt{2}L. \tag{2.3}$$

This leads to a volume of the solid closed cell, which is composed of six square faces and eight hexagonal faces,

$$V_s = \frac{t}{2}\left(6A_{\text{rect}} + 8A_{\text{hex}}\right) = 3tL^2\left(1+2\sqrt{3}\right). \tag{2.4}$$

Dividing by the total volume of the regular Kelvin cell, $V = HD^2 = 16\sqrt{2}L^3$, the face thickness t is constrained by the foam relative density, $\frac{\rho}{\rho_s}$, and the face length:

$$\frac{\rho}{\rho_s} = \frac{V_s}{V} = \frac{3t\left(1+2\sqrt{3}\right)}{16\sqrt{2}L}. \tag{2.5}$$

The thickness is then a simple function of the relative density:

$$t = \frac{16\sqrt{2}L\,\rho/\rho_s}{3\left(1+2\sqrt{3}\right)}. \tag{2.6}$$

As the volume of the cells was measured in the preceding sections and not the face length, a final constraint is provided by substituting the face length L for the cell volume V measured by the *Extended Particle Analyzer*. This leads to a face thickness $t = 0.0185$ mm for the regular, isotropic Kelvin cell with a relative density of 0.077.

As has been noted above, the microstructure is anisotropic, and there is concentration of material in the nodes of the D-H100 cells. To model the cell structure more accurately, the material concentration in the nodes is modeled as a set of expanding spheres centered at the vertices of the Kelvin cell, and the cell dimensions are stretched in the rise direction to fit a given anisotropy parameter $\lambda = H / D$. Fig. 2.10 shows the modified geometry in the expanded model with spheres of radius $R = 0.15L$.

The volume of solid foam material in a cell for spheres of radius R is then given by (Appendix A),

$$V_s = t\left(b^2 + 2L^2 + 8bL\sin\phi + 8L^2\sin\phi\cos\phi\right) + 8\pi R^2\left(R - t\right). \tag{2.7}$$

The expression for the face thickness is obtained as,

$$t = \frac{4L\sin\theta\left(2L\cos\theta + \sqrt{2}b\right)^2\frac{\rho}{\rho_s} - 8\pi R^3}{b^2 + 2L^2 + 8bL\sin\phi + 8L^2\sin\phi\cos\phi - 8\pi R^2}. \tag{2.8}$$

The face thickness is now a function of both the foam relative density, ρ/ρ_s, and the radius of the spheres, R, representing the concentration of foam material in nodes.

Defining the cell volume, anisotropy, and relative density leaves face thickness a function of only the material concentration in the nodes, or alternatively, the fraction of solid material in the spheres,

$$\frac{V_{\text{spheres}}}{V_s} = \frac{8\pi R^3}{t\left(b^2 + 2L^2 + 8bL\sin\phi + 8L^2\sin\phi\cos\phi\right) + 8\pi R^2\left(R - t\right)}. \tag{2.9}$$

Fig. 2.11 shows the relationship of face thickness between the fraction of solid material concentrated in the nodes for a relative density $\rho/\rho_s = 0.077$ for an isotropic Kelvin cell and a Kelvin cell with the observed anisotropy $\lambda = 1.4$. In this idealized model, the face thickness reduces approximately linearly with an increase in material concentration in the nodes. It is also observed that assuming a uniform face thickness, a more anisotropic cell has a smaller face thickness for a given material concentration in the nodes.

	l_{xy}	l_{xz}	l_{yz}
μ	1.0	1.4	1.4
σ	0.21	0.29	0.29

Table 2.2: The mean anisotropy parameters in each direction pair and their standard deviations.

	Data		Lognormal Distr.		
	μ	σ	mean	mode	st. dev.
D	0.501	0.092	0.501	0.476	0.094
t	0.0348	0.018	0.0354	0.0222	0.0213

Table 2.1: Fits of the data and lognormal distributions for cell diameter and face thickness in millimeters.

(a)

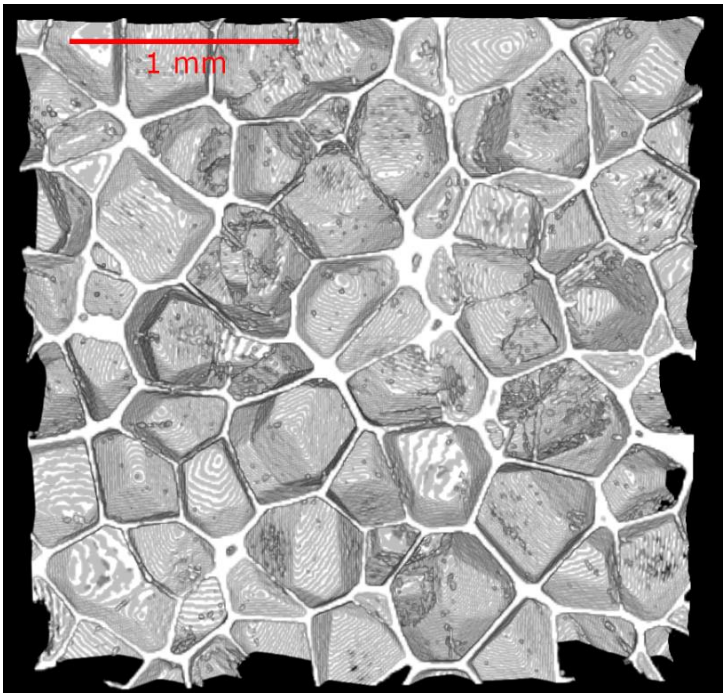

(b)

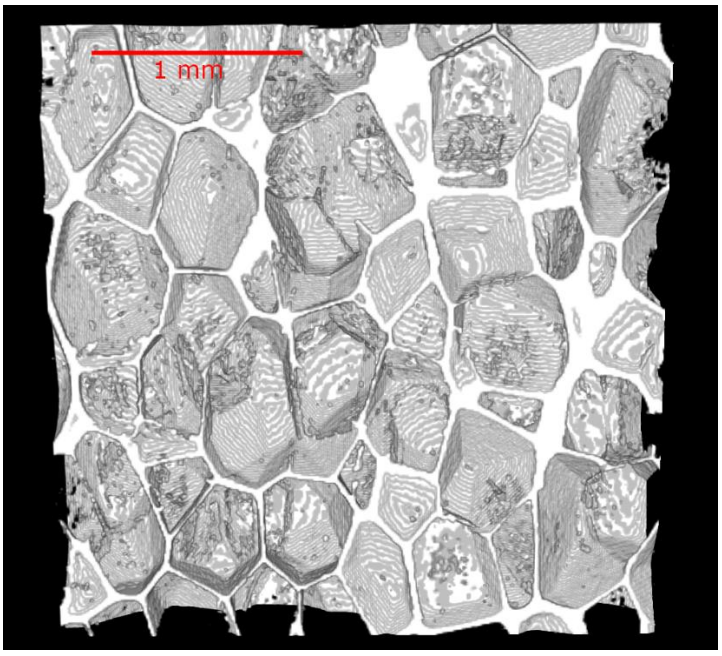

Figure 2.1: X-ray tomography planar images showing the polyhedral cell distribution of D-H100 closed-cell foam. (a) Plane normal to the rise direction and (b) plane along the rise direction.

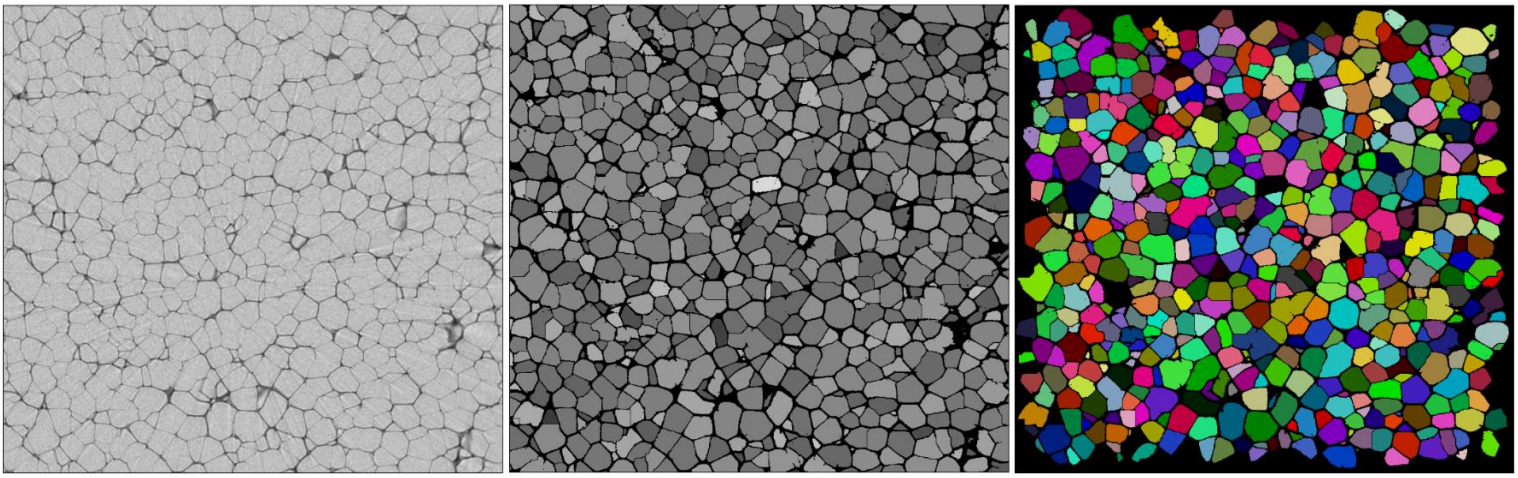

(a) (b) (c)

Figure 2.2: (a) A slice of the 3-dimensional TIFF data collected by the µCT 80 machine. (b) The same data after thresholding and watershed segmentation. (c) The particles identified by the Extended Particle Analyzer from the watershed segmented data.

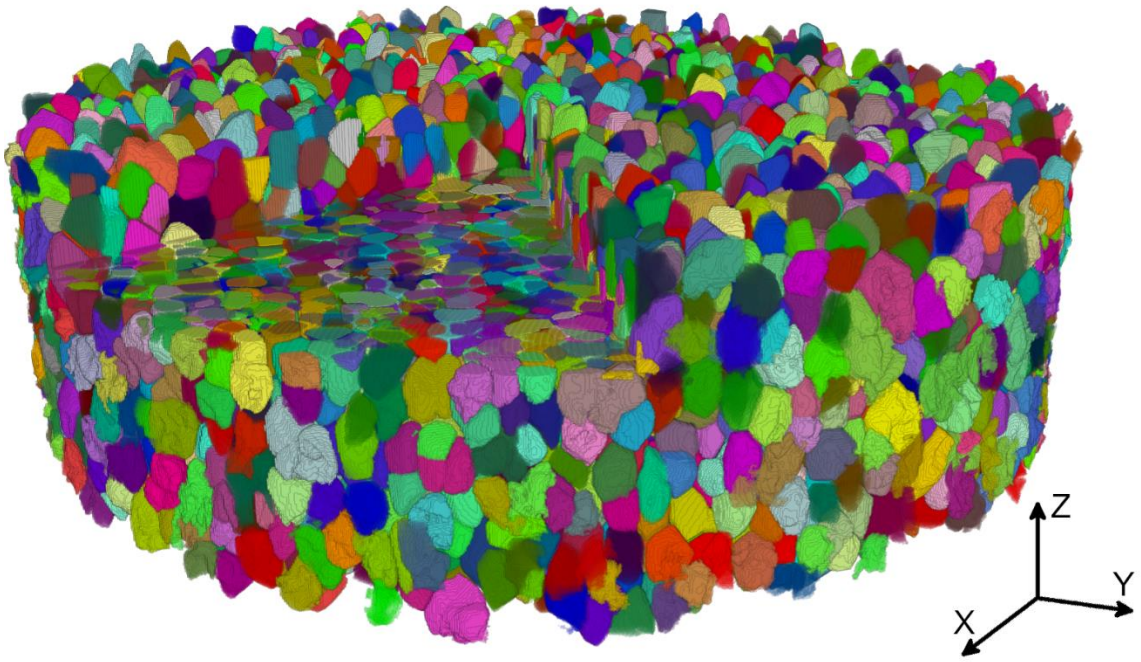

Figure 2.3: 3-D rendering of cell volumes in the D-H100 closed-cell foam identified by the *Extended Particle Analyzer*.

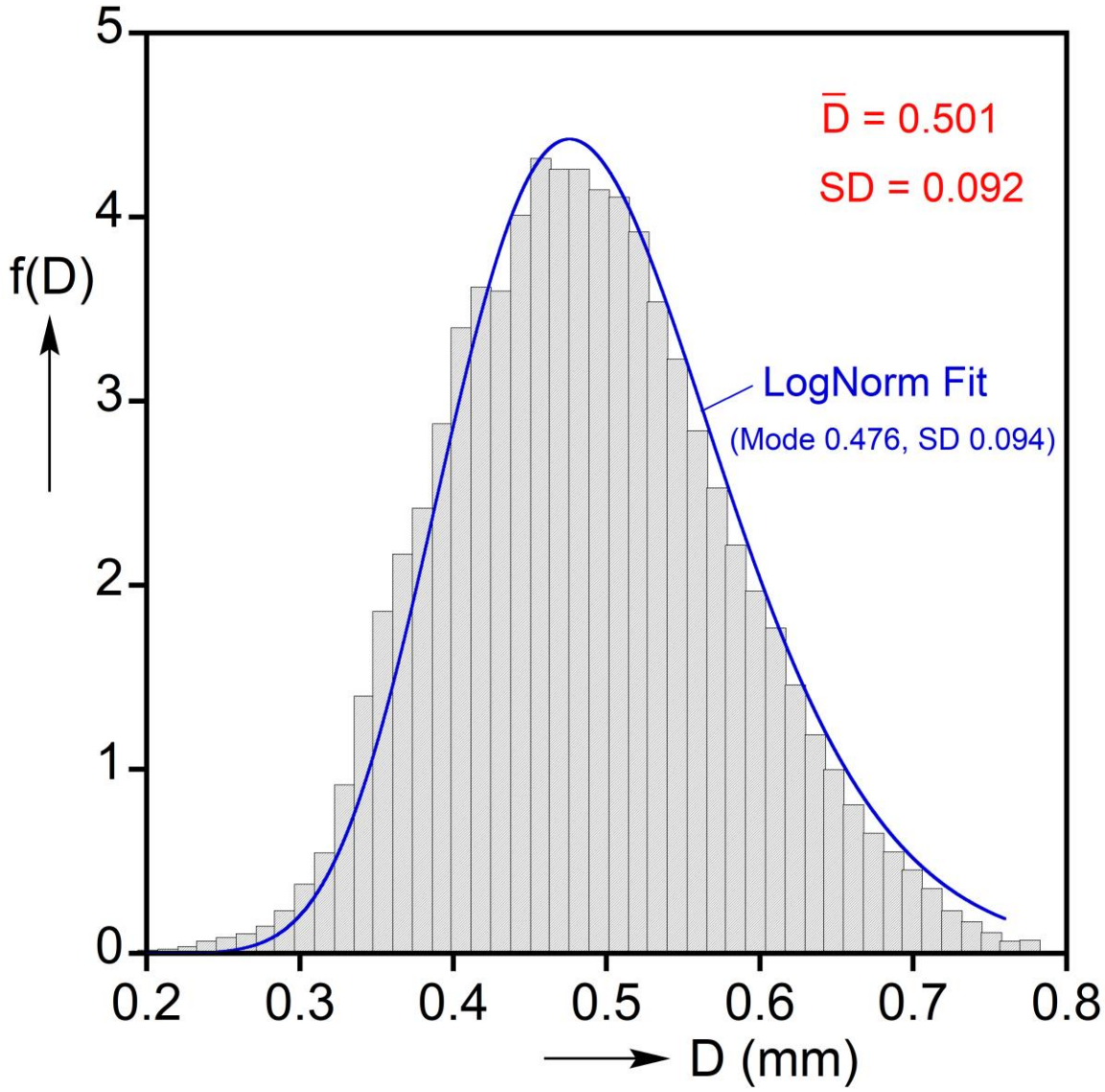

Figure 2.4: The cell diameter distribution and the least squares lognormal fit to the data.

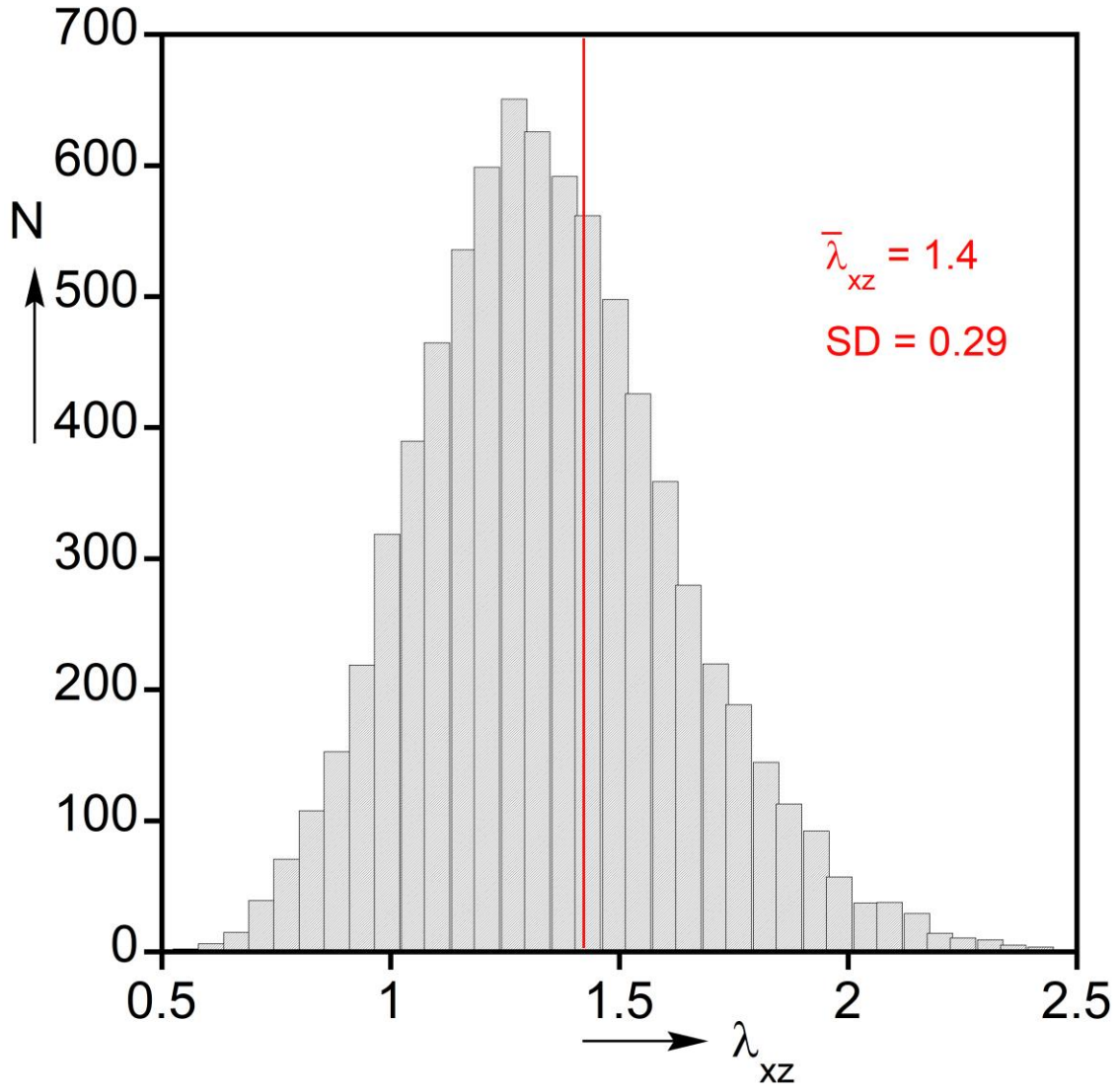

Figure 2.5: Distribution of the cell anisotropy measure λ_{xz} .

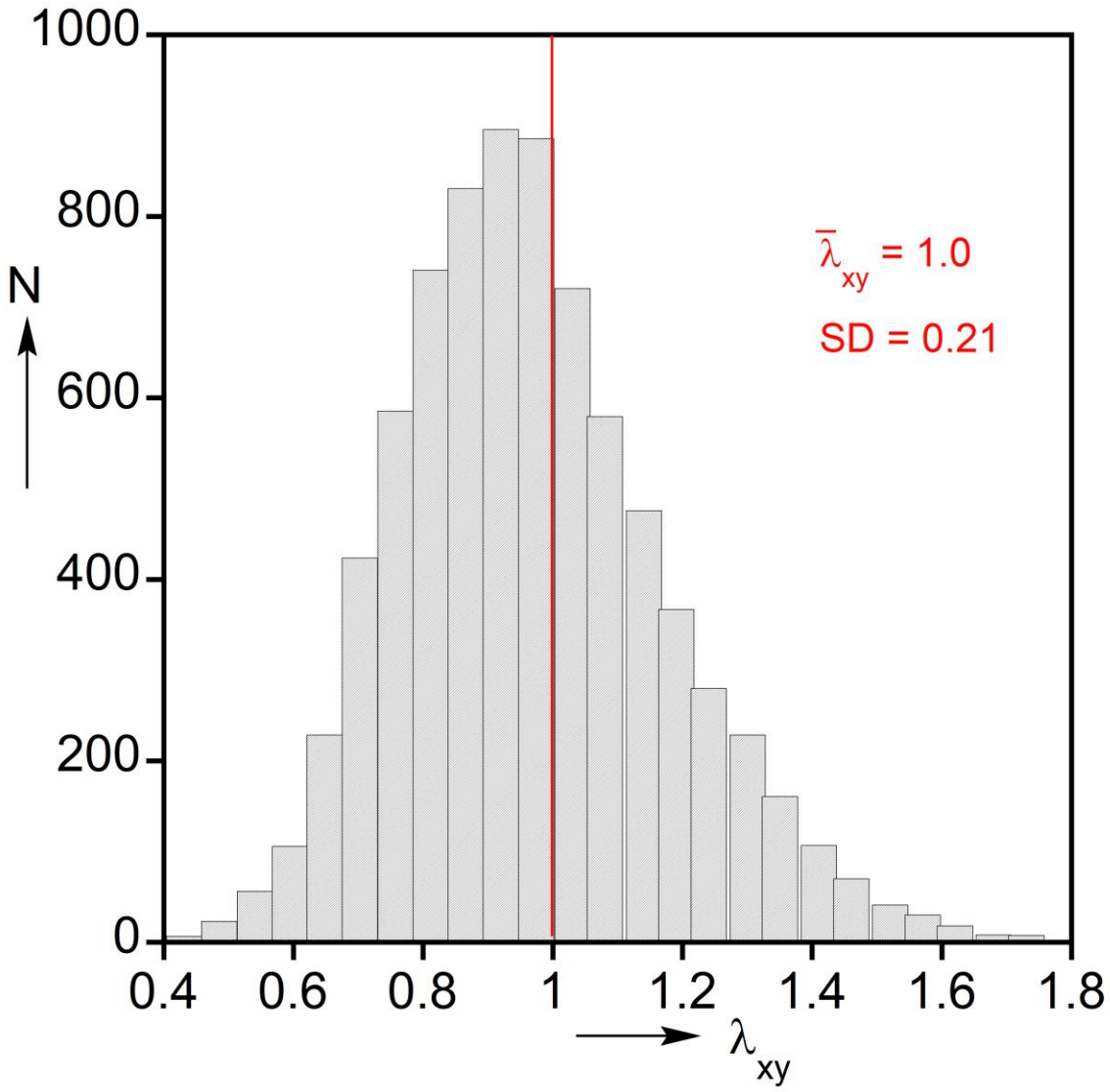

Figure 2.6: Distribution of the cell anisotropy measure λ_{xy}.

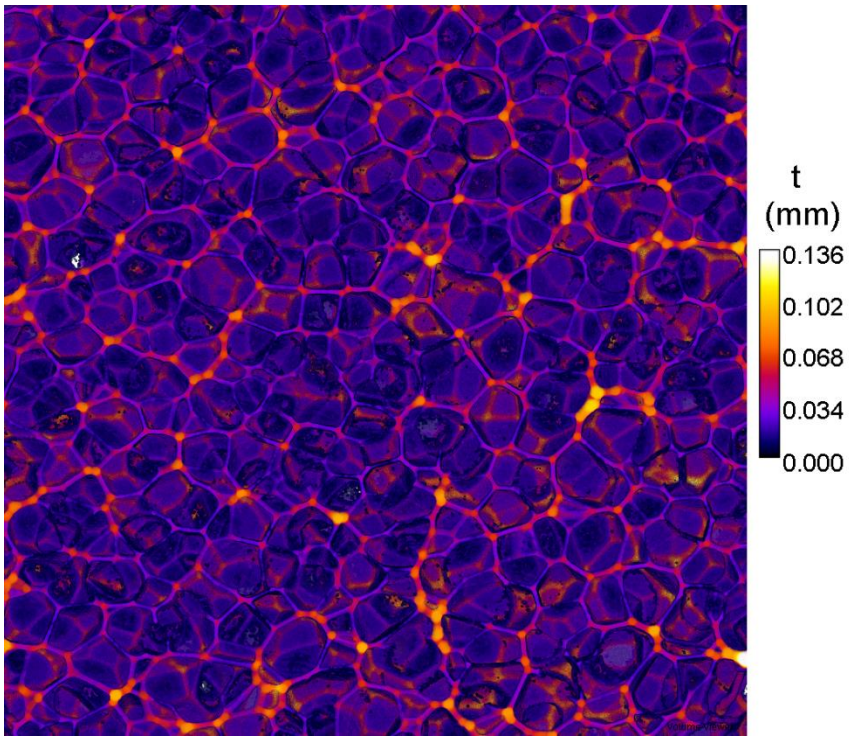

Figure 2.7: A 3-D visualization of the face thickness distribution as computed from a μCT scan of the Divinycell H100 foam using the *Local Thickness* software.

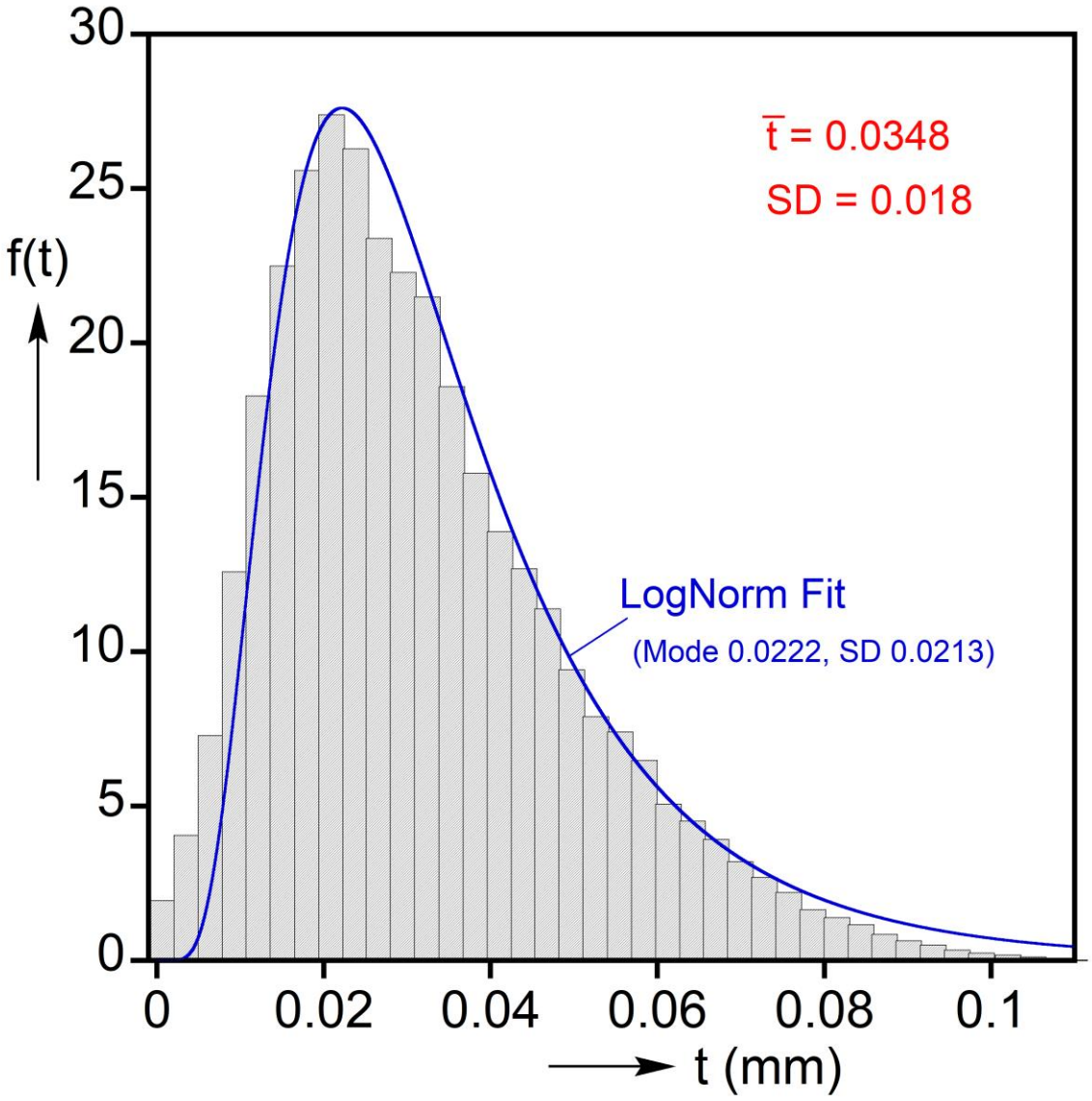

Figure 2.8: The cell wall thickness distribution and a lognormal fit to the data.

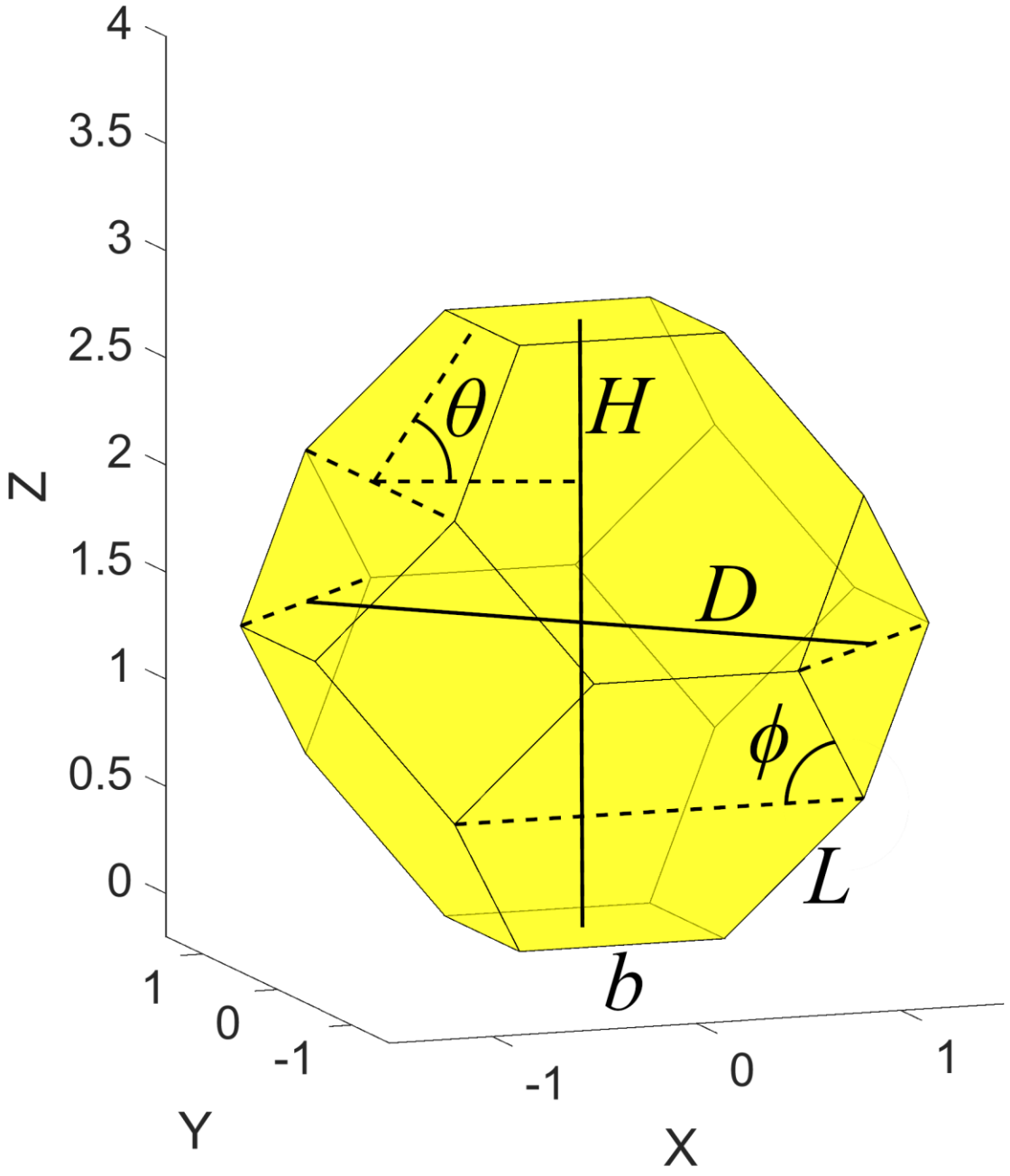

Figure 2.9: A regular Kelvin cell with labeled diameter (D), height (H), hexagon tilt angle (θ), and hexagon interior angle (ϕ).

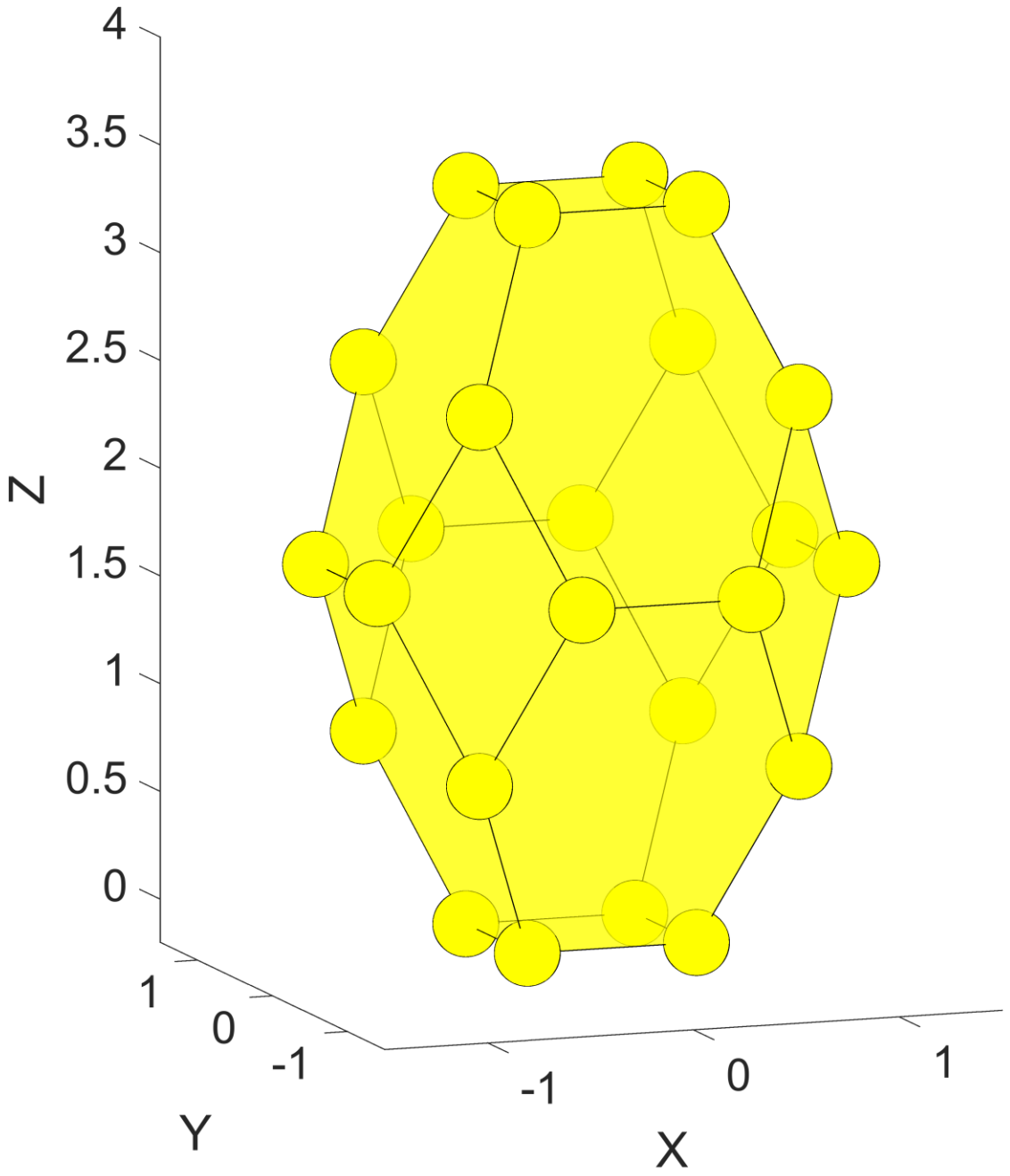

Figure 2.10: A Kelvin cell elongated to anisotropy $\lambda = 1.4$ with sphere radius $R = 0.15L$, corresponding to a sphere volume fraction $\frac{V_{sphere}}{V_s} = 0.0626$.

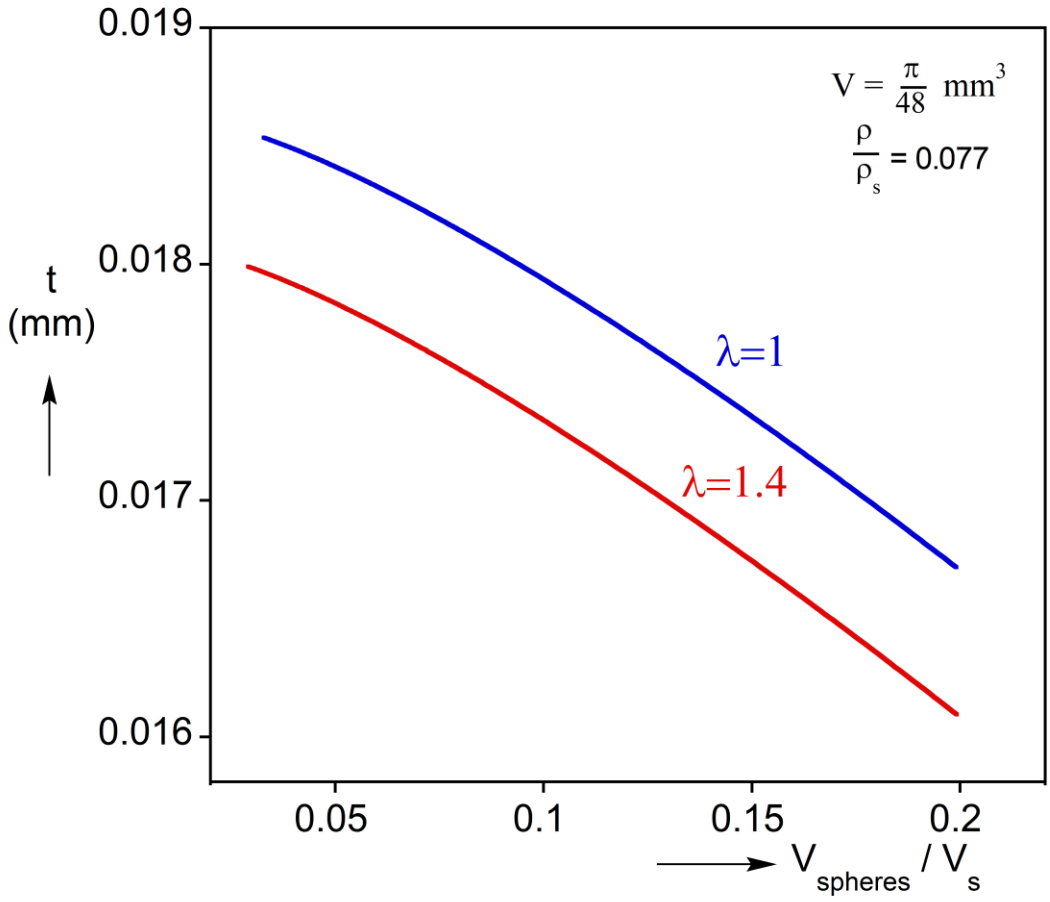

Figure 2.11: The dependence of face thickness on sphere volume fraction with and without the observed anisotropy for the Kelvin cell model with a cell size of 0.5 mm ($V = \frac{\pi}{48}$ mm^3) and a relative density $\frac{\rho}{\rho_s} = 0.077$.

Chapter 3: Experimental Setup

A custom triaxial testing apparatus was designed and fabricated to conduct loading experiments on Divinycell H100 closed-cell polymeric foam. The full test apparatus assembly is shown in Fig. 3.1. This assembly consists of a pressure chamber made of a transparent acrylic tube capped by aluminum flanges. An internal, custom-made brass load cell connects to a specimen-end cap assembly. The specimen is compressed via a rod that penetrates the top flange as shown in the figure. The chamber is pressurized by compressed air through a pressure regulator. A pressure transducer monitors the pressure. This chapter describes the test apparatus in detail together with the diagnostics and data acquisition used.

3.1 Specimen Fabrication and Preparation

The test specimens used in crushing experiments were 38.1 mm (1.50 in) diameter, 51 mm (2.0 in) tall cylinders of Divinycell H100. The axial direction of the compression corresponds to the rise direction of the foam. The foam specimens were milled out of a 51 mm thick mother plate. Thus, the specimens covered the full thickness of the mother plate. A view of a typical Divinycell H100 foam specimen is shown in Fig. 3.2. Steel end caps were bonded to the ends of each specimen, through which it engaged the test fixture. A thin rubber membrane was used to cover the test specimen and end plugs assembly to avoid penetration of compressed air into the specimen (see Fig. 3.1). The thickness of the membrane was approximately 0.11 mm (0.0045 in).

3.2 THE PRESSURE CHAMBER

The pressure chamber consists of a transparent cast acrylic tube that surrounds the test specimen. It has a diameter of 150 mm (6 in), wall thickness of 19 mm (0.75 in), and height of 180 mm (7.1 in). It is closed with 19 mm (0.75 in) thick aluminum flanges each with a small aligning recess matching the acrylic tube. O-rings resting in grooves machined into the flanges are used to seal the chamber. The chamber is held closed by four stiff steel bolts. It is pressurized using compressed house air supplied though an inlet in the top flange. The pressure is maintained at the required level using a pressure regulator, while the rate of pressurization is controlled by a fine valve. The pressure is monitored by a pressure gage and a pressure transducer with a pressure range of 69 bar (1000 psi). The calibration voltage response to pressure of the transducer is shown in Fig. 3.3.

An elastic analysis was used to select the wall thickness of the acrylic chamber. It was designed to have a pressure capacity of 13.8 bar (200 psi) with a safety factor of about 10. The analysis in Appendix B produced the following relationship between the pressure at yield, P_y, and the yield stress of the acrylic, σ_y:

$$P_y = \frac{r_o^2 - r_i^2}{\sqrt{3r_o^4 + (1 - 2\nu)^2 r_i^4}} \sigma_y , \tag{3.1}$$

where r_o and r_i are the outer and inner radii of the tube and ν is Poisson's ratio. The properties of the acrylic tube are listed in Table 3.1.

Again using the elastic analysis in Appendix B, the radial displacement of the outer edge of the thick-walled pressure vessel is given by,

$$u_r\left(r_o\right)=\frac{2pr_i^2r_o\left(1-\nu\right)\left(1+\nu\right)}{E\left(r_o^{\,2}-r_i^2\right)}. \tag{3.2}$$

At the maximum design pressure of 200 psi, this leads to a diameter expansion $\Delta D=2u_r(r_o)\approx 0.15$ mm (0.0059 in). The diameter expansion of the acrylic tube under maximum design pressure was used to set the size of the groove in the aluminum flanges in which the acrylic tube rests.

3.3 The Custom Load Cell

The axial loading on the foam specimen was monitored using a custom brass load cell designed to be operated inside the pressure chamber to avoid frictional effects between the loading rod and the O-ring seal at the entrance of the chamber. The load cell consists of a 38.1 mm (1.5 in) diameter brass shell with a wall thickness of 0.508 mm (0.020 in). The brass shell is bonded to brass end caps at the top and bottom via small grooves (Fig. 3.4a).

Four strain gages connected to a full bridge for maximum sensitivity are placed on the outer surface of the cylinder, as shown in Fig. 3.4 and 3.5. Appendix C demonstrates that the arrangement is self-temperature compensating and is insensitive to bending. The strain gages used have gage factor 2.12 and excitation 5 V. The voltage output of the bridge is continuously monitored via a LabVIEW data acquisition system and by an analog voltmeter. The load cell was calibrated by applying compression up to

1110 N (250 lb) via a calibrated load cell connected to the same testing machine. Fig. 3.6 shows the calibration of the brass load cell by its voltage response to axial load.

The thickness of the brass shell was selected based on yielding and buckling analysis for a thin-walled tube. From this analysis, the yield and buckling loads, F_y and F_c, are given in terms of the shell material parameters in Eqs. (3.3) and (3.4):

$$F_y = 2\pi R t \sigma_y, \tag{3.3}$$

$$F_c = \frac{2\pi E t^2}{\sqrt{3\left(1-\nu^2\right)}}, \tag{3.4}$$

where t is the thickness of the shell, R is the radius of the shell cylinder, and σ_y, E, and ν are the yield stress, Young's modulus, and Poisson ratio of the brass alloy respectively.

Table 3.2 shows the properties of the 260 brass with H80 temper used in the load cell. In designing a load cell for axial deformation, the most important consideration is that the loads at which the load cell operates should cause an elastic strain large enough to be captured by the strain gage configuration while safely avoiding yield and buckling. For this material, the minimum thicknesses for a yield safety factor of 2 and a buckling safety factor of 5 as calculated by Eqs. (3.3) and (3.4) for a design load of 4448 N (1000 lb) are shown in Fig. 3.7 with the associated strain as a function of tube thickness. The true 0.508 mm (0.020 in) thickness of the load cell leads to a strain of $\varepsilon_z \approx 0.0007$ at the maximum design load with a safety factor in yield of approximately 2.

3.4 Assembly and Experiment Preparation

A laser non-contact extensometer with a measurement range of 8 to 127 mm (0.5 – 5 in) and a maximum resolution of 0.001 mm (0.00004 in) is used to monitor the displacement of the specimen using reflective targets placed on the steel end caps. The signal is recorded directly in LabView on a common time base with the load cell, pressure transducer, and machine displacement signals.

Installation begins by bonding the specimen to the top and bottom surfaces of the end caps. The load cell is connected to the loading rod that penetrates through the upper flange. The specimen and end caps are connected and aligned with the load cell using an all-thread connector. The top flange assembly is then lowered into the chamber so that the bottom of the specimen rests on the bottom flange. The chamber is secured in place by tightening nuts on the four steel rods. The machine crosshead is then moved upwards until the loading rod comes into contact with the stationary crosshead through a close-fitting access hole that ensures the system is aligned. While the machine is moved, the load is monitored to limit frictional loading that may be applied to the sample before the experiment begins.

After alignment, the chamber is pressurized to the required level, and the pressure is kept constant as the specimen is compressed. During the pressurization, the change in load and pressure are monitored through the DAQ system. The laser extensometer gage length, the load cell load zero, and the pressure transducer pressure zero are recorded prior to the beginning of pressurization. The specimen is then

compressed at a strain rate of 2×10^{-4} s^{-1} (this corresponds to the uniform deformation stage).

A Nikon D90 DSLR 12-megapixel camera monitors the overall deformation of the test specimen during the initial pressurization and throughout the compression history, taking pictures at a programmed time interval. Typically, the camera was programmed to take pictures at a rate of one picture per minute. Post-experiment pictures were also taken of each specimen after it was removed from the chamber to capture the failure zone in more detail.

Property	Value/Unit
Material	Cast Acrylic
Yield Stress	64.8 MPa – 82.7 MPa (9.4 – 12 ksi)
Modulus of Elasticity	2758 – 3303 MPa (400 – 479 ksi)
Poisson's Ratio	0.37
Dimensions (D× H)	152.4× 177.8 mm (6× 7 in)
Tube Thickness	19.0 mm (0.75 in)
Maximum Pressure	13.8 bar (200 psi)

Table 3.1: Properties of the cast acrylic tube used as a pressure vessel.

Property	Value/Unit
Material	260 Brass H80 (ASTM B135)
Yield Stress	439.9 MPa (63.8 ksi)
Modulus of Elasticity	110 GPa (16000 ksi)
Poisson's Ratio	0.375
Dimensions (D× H)	38.1× 50.8 (1.5× 2 in)
Tube Thickness	0.508 mm (0.02 in)
Load Capacity	4448 N (1000 lb)

Table 3.2: Properties of the brass tube used in the custom load cell.

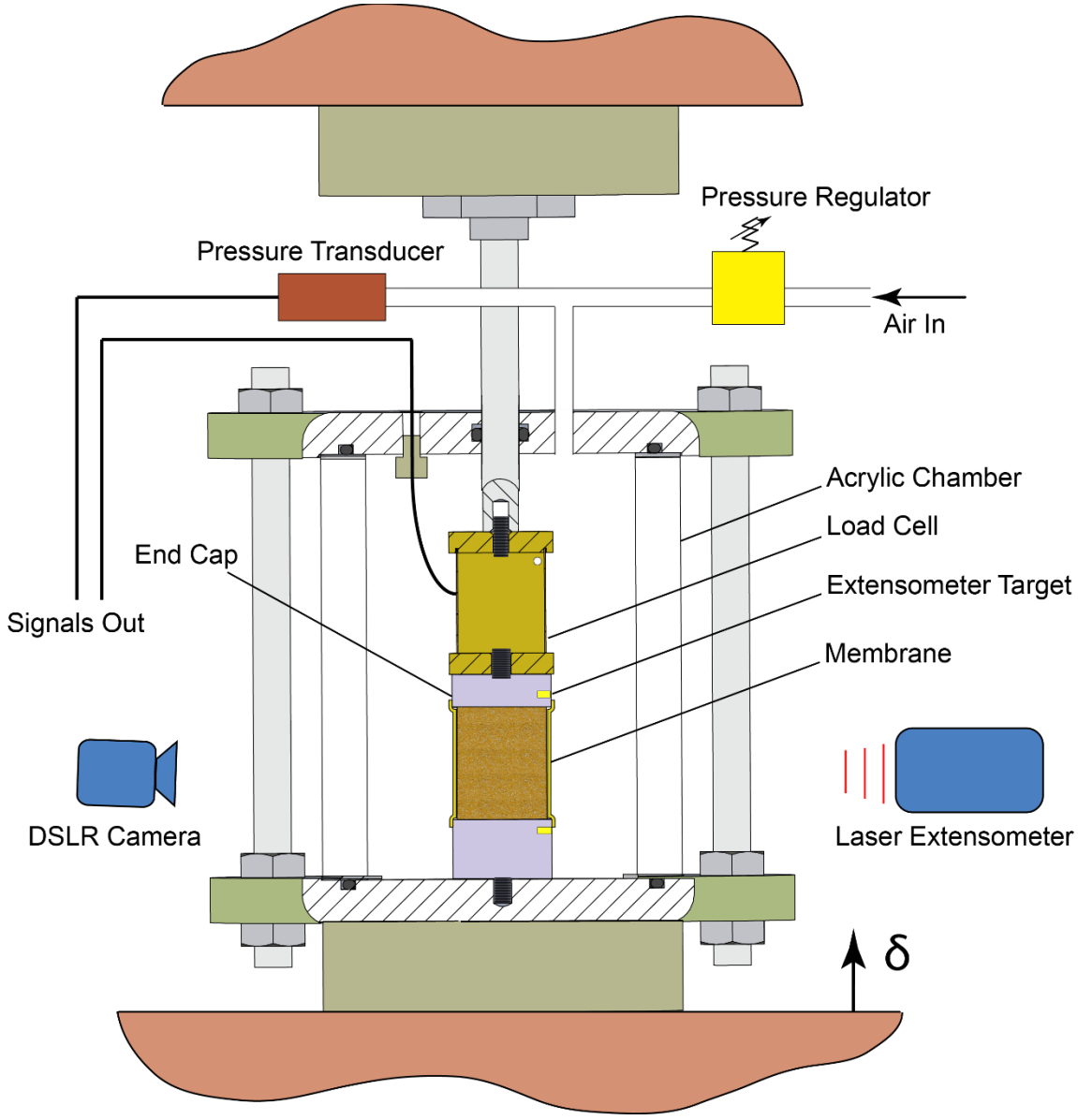

Figure 3.1: Scaled schematic of the triaxial test setup used in the experiments with major components identified (transparent acrylic chamber diameter = 150 mm).

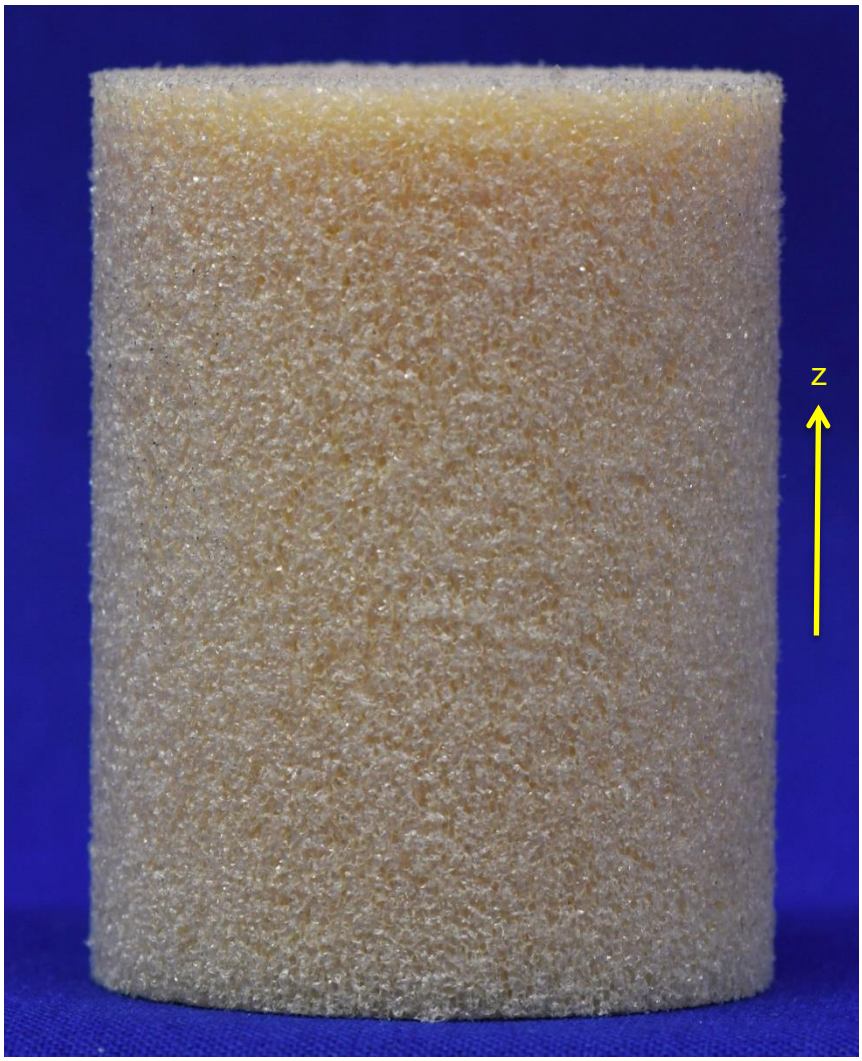

Figure 3.2: A cylindrical specimen of Divinycell H100 closed-cell foam with the rise direction labeled as the z-axis.

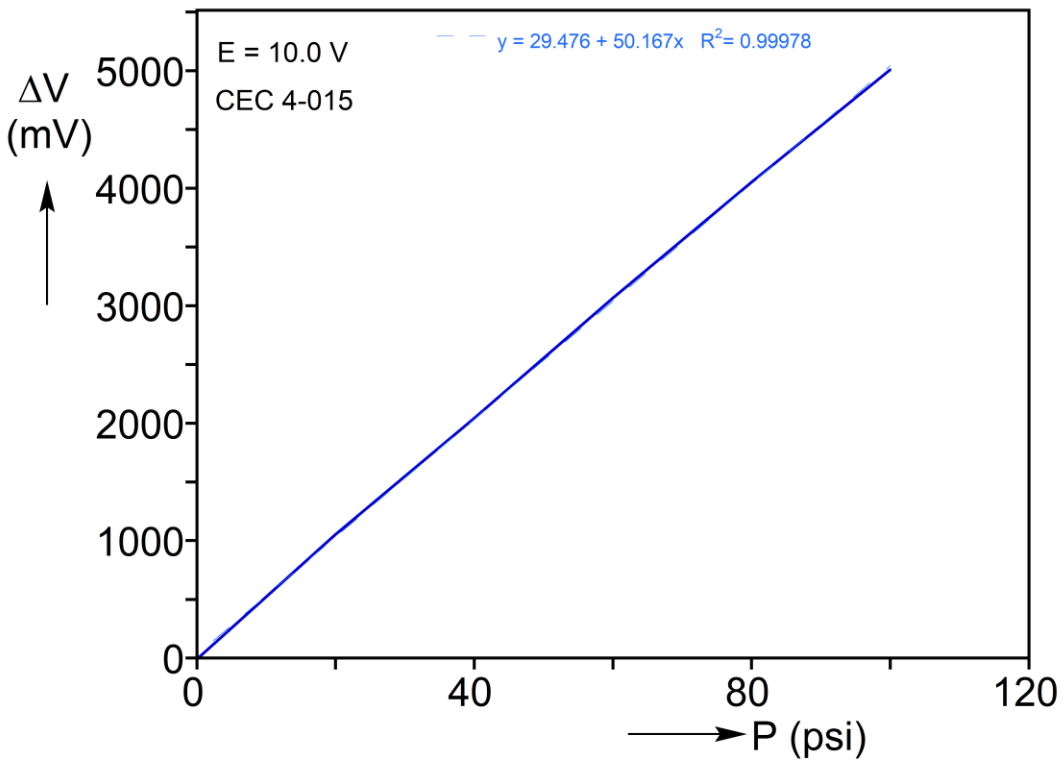

Figure 3.3: The calibration curve for the pressure transducer.

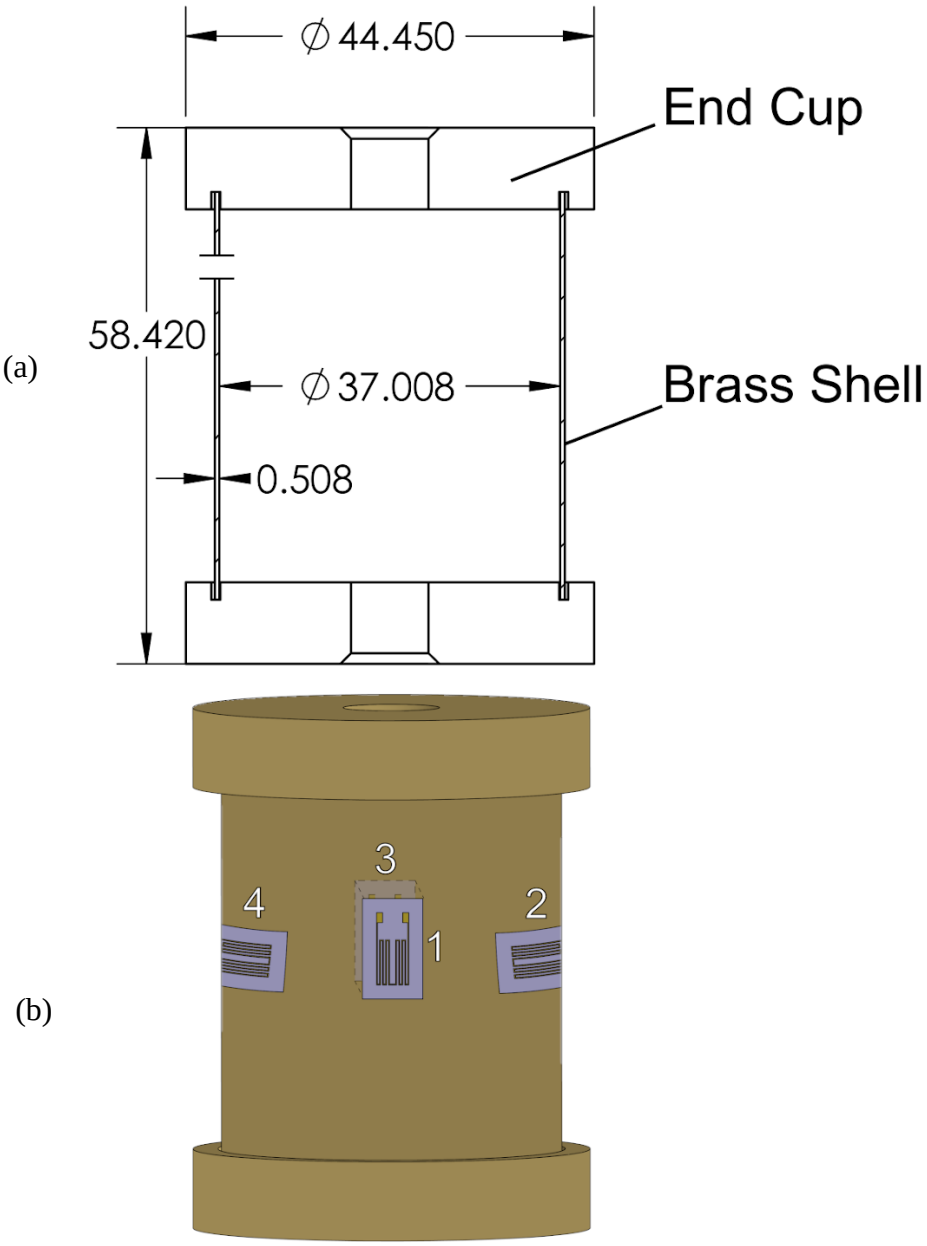

Figure 3.4: (a) The dimensions of the load cell assembly in mm, including the brass shell and the two end caps with through holes. To avoid pressure loading on the brass shell, a small hole was drilled through the shell wall. (b) The placement of strain gages 1, 2, 3, and 4 on the brass shell.

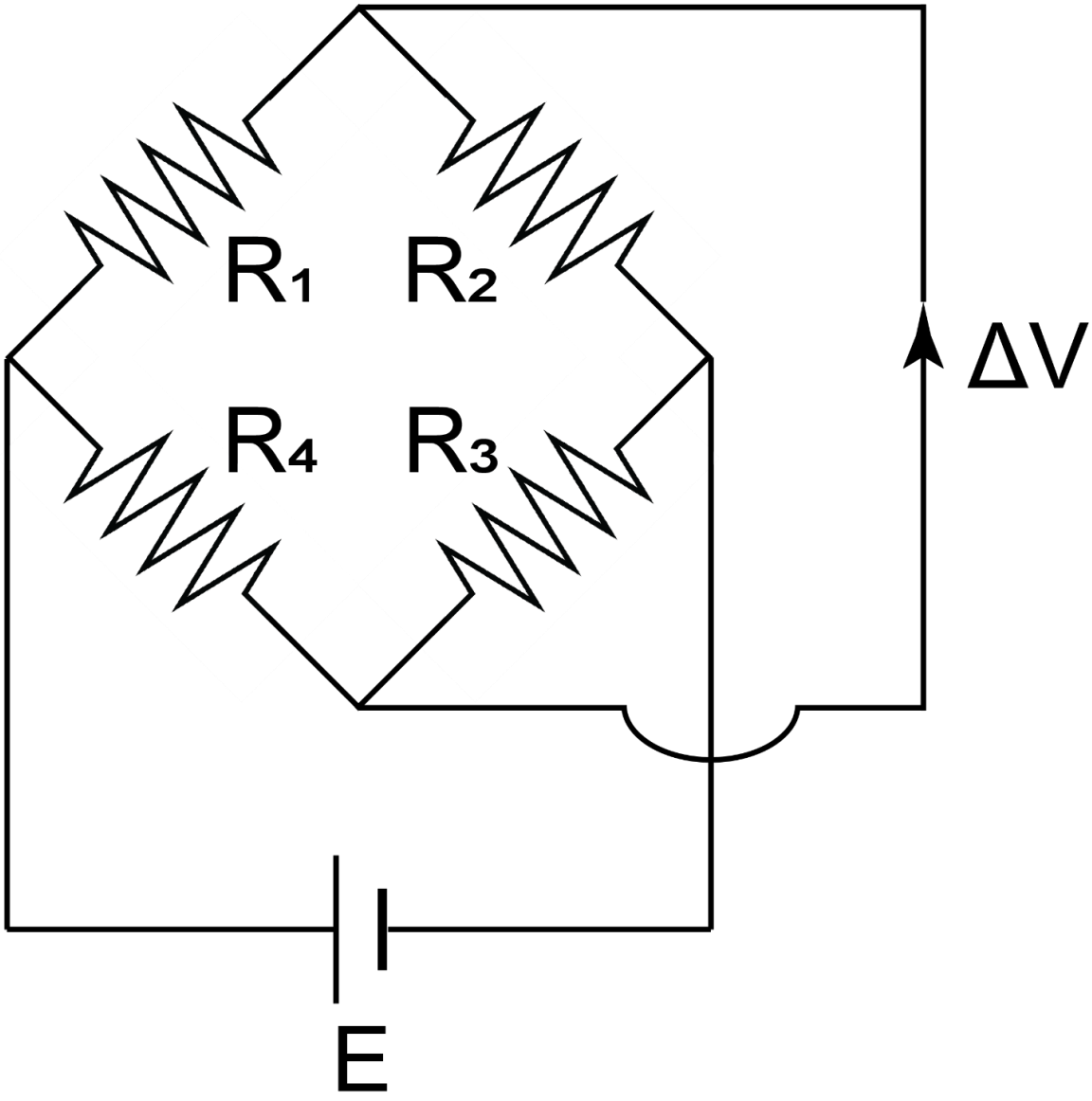

Figure 3.5: A schematic of the Wheatstone bridge used in the custom brass load cell to compensate for temperature and bending loads.

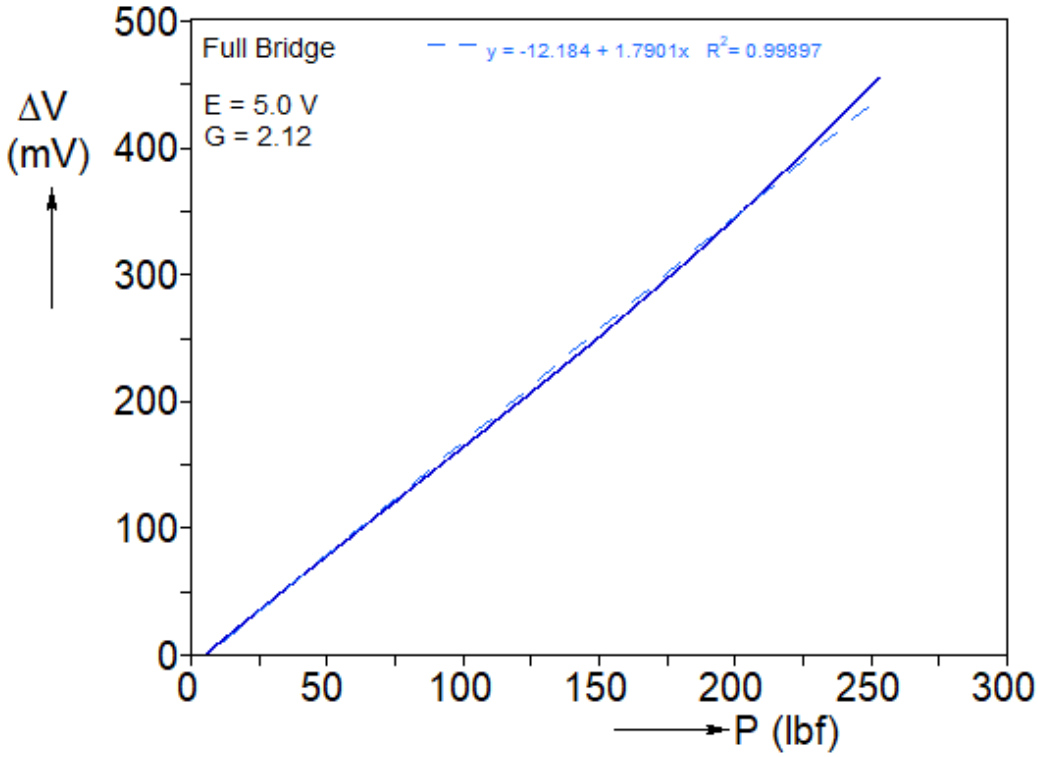

Figure 3.6: The calibration curve for the custom brass load cell.

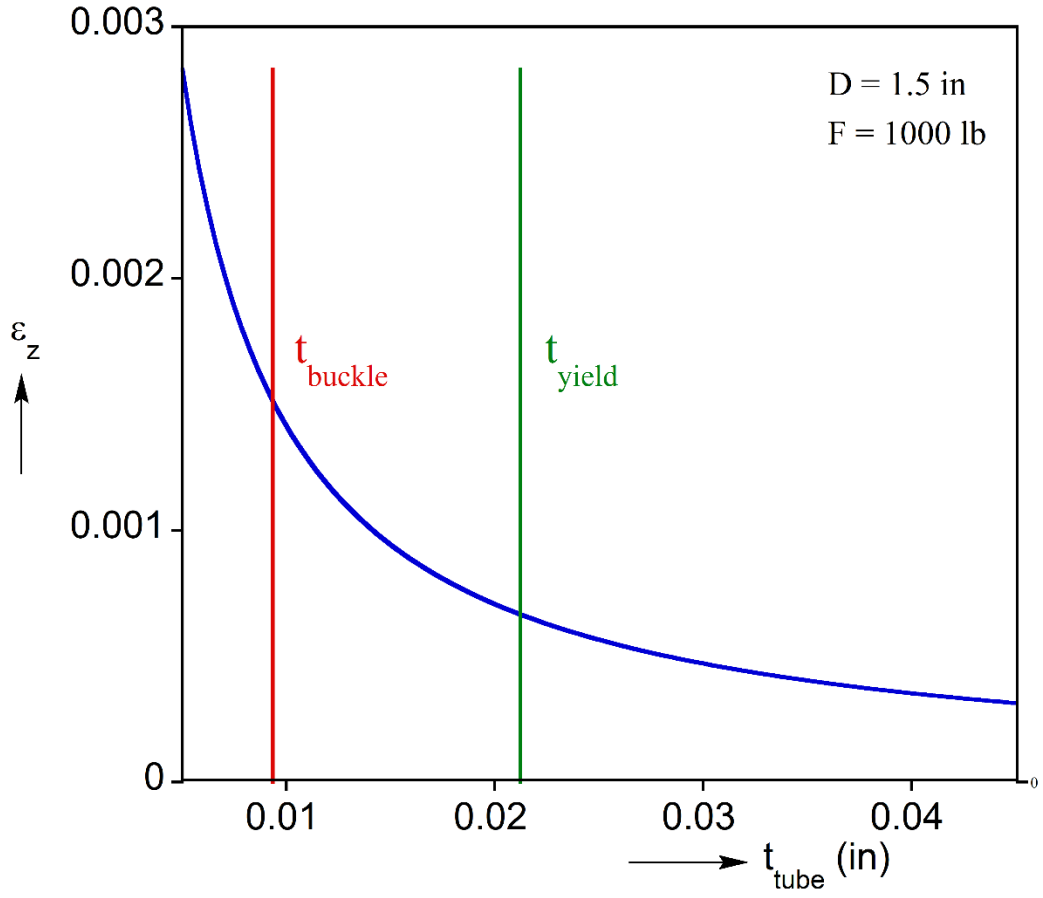

Figure 3.7: The thickness required to support a load of 4448 N (1000 lb) for the H80 brass tube used in the load cell based on buckling (safety factor 5) and yielding (safety factor 2).

Chapter 4: Triaxial Experiments

The deformation of the closed-cell PVC foam (Divinycell H100) with a relative density of 7.7% under triaxial loading was investigated in a series of experiments described in this chapter. The specimens were pressurized to a selected level and then compressed at a typical displacement rate of 0.005 mm/s (0.0002 in/s), which induces a strain rate of $\dot{\varepsilon} \approx 10^{-4}$ s^{-1} to a uniformly deforming specimen.

A separate experiment was conducted on a smaller specimen, which was crushed under pure compression. This test was stopped periodically to capture the evolution of crushing using 3-D computed X-ray tomography.

In the course of the triaxial experiments, it was noticed that the crushing behavior changes at higher pressure levels. This prompted separate experiments in which the specimen was loaded under pure external pressure.

4.1 Triaxial Crushing of Divinycell H100

The results of Exp. FM11 in which the foam was compressed at a pressure $P =$ 6.17 bar (89.4 psi) will be used to discuss the general trend of the behavior observed. Plotted in Fig. 4.1a is the recorded nominal axial stress-shortening, σ - δ / H, response, where σ is the net axial compressive stress with the effect of the pressure removed, and H is the initial height of the specimen – compressive stress is positive throughout this manuscript. Initially, the stress rises linearly with an elastic modulus of about 80 MPa (11.5 ksi). For stress higher than 0.65 MPa the response becomes progressively more nonlinear, reaching a maximum of $\sigma_I =$ 1.14 MPa (165 psi) – *initiation stress*. Using a

strain offset of 0.15% the yield stress, S_o, is 1.08 MPa (157 psi). Following the maximum, the stress drops sharply down to a small transient that eases into an extended plateau indicative of a steady-state evolution of events. The response was terminated at an average strain of about 15%, and the level of the plateau stress, S_P, averaged over a strain extent of 12.8% is 0.83 MPa (120 psi).

Fig. 4.1b shows a set of overall images of the specimen recorded at 60 s intervals during the stress plateau. Six images are shown that correspond to the numbered solid bullets marked on the response. The load maximum is indicative of an instability, which for this foam specimen leads to localization of deformation that can be seen at a more progressed stage in image ① at an average strain of 5%. Deformation has localized in a narrow zone approximately at the specimen mid-height. The zone of localization, although somewhat jagged, is essentially normal to the axial load and covers the whole circumference. The local deformation causes the protruding wrinkle in the rubber membrane that surrounds the foam. Experience has taught that deformation tends to initiate at a neighborhood of "weaker" cells with reduced rigidity. Here it takes the form of crushed cells that destabilize their neighbors with crushing quickly spreading across the specimen. Persistent compression causes the nearly horizontal band to propagate axially. Concurrently, material outside this zone remains essentially intact. The progressive broadening of the crushing zone is illustrated in images ② to ⑥, which respectively correspond to average strains of {6.82, 8.62, 10.4, 12.2, 14.0}%.

A clearer view of the localization zone is provided in Fig. 4.1c, which shows the specimen unloaded at the end of the test with the rubber membrane removed. The band of crushed cells is somewhat ragged but nearly axisymmetric. Interestingly, the band has contracted radially, forming a nearly parabolic edge profile. The lateral contraction is caused by the applied triaxial compressive stress state, as it does not develop in the absence of or at low levels of pressure. It appears that as new rows of cells become destabilized by the axial compression, they also become more compliant to lateral pressure, resulting in the observed radial deformation in the crushed zone.

4.2 TESTING AND SCANNING OF A SMALLER SPECIMEN

To investigate the behavior of the foam microstructure during pure axial compression, a separate experiment was conducted in which the evolution of crushing under zero pressure was monitored using X-ray tomography. The limitations of our μCT 80 system dictated that the specimen be crushed outside the scanner and transferred to it for scanning. Furthermore, for more efficient scanning, the foam specimen size was reduced to a cylinder with 22 mm (0.865 in) height and 15.2 mm (0.60 in) diameter milled out of the mother plate along the rise direction. Tight fitting end caps were again lightly bonded to the specimen, and the assembly was compressed in the same apparatus (Fig. 3.1).

The specimen was compressed at the same rate of $\dot{\delta}/H = 10^{-4}$ s^{-1} with the shortening again monitored by a non-contact laser extensometer. The crushing experiment was interrupted several times for the specimen to be removed from the

apparatus and transferred to the μCT80 for scanning. The scanning typically took about two hours and, since the foam material is rate dependent, upon unloading the specimen was placed in a special holder that kept it at the crushed height during scanning. The holder, shown in Fig. 4.2, consists of a 35 mm (1.375 in) diameter polycarbonate tube with a threaded internal diameter of 22.5 mm (0.875 in). The bottom is closed, and the specimen is held to length by a polycarbonate threaded plug as shown in the figure. A shaped steel rod at the bottom of the holder is used to engage the scanner sample stage. The scans were performed with a voxel size of 10 μm and covered the whole cylindrical specimen.

Fig. 4.3a plots the nominal stress vs. the shortening of the specimen normalized by the initial height. The stress traces an extended plateau characteristic of propagating instabilities. The stress plateau is approximately at the same level as that of the larger specimen in Fig. 4.4. The usual initiation peak has been masked, most likely by some imperfection at the lower end where crushing apparently initiated. The numbers in circles mark the points on the response where a scan was performed. Fig. 4.3b depicts samples of the results of the scans that consist of full height 10 μm thick slices through the center of the specimen. Image ⓪ corresponds to the undeformed specimen with approximately 30 cells across and 40 along the height. It displays the relatively low polydispersity cell distribution, and the cell elongation in the axial/rise direction reported in Section 2.2.

Images ①, ② and ③ show the specimen at different stages of crushing. The slices originated approximately from the same section through the specimen. Image ① shows the specimen at approximately 26% average strain. Crushing is seen to have initiated at

the lower end and propagated upward. Most of the deformation has been absorbed by a zone that represents approximately 20% of the initial height. The zone consists of heavily deformed and crushed cells, some organized in bands with small random inclinations, which is consistent with the behavior observed in open-cell foams (Fig. 10, Jang and Kyriakides, 2009). Furthermore, the width of the crushed zone appears nearly unchanged. Concurrently, the rest of the specimen appears essentially undeformed. Attributing all displacement supplied to this zone leads to an average strain in the crushed zone of approximately 50%.

In image ② the specimen is at an average strain of about 40%. The crushed zone has propagated upward covering nearly 27% of the specimen. The front separating the highly deformed and the nearly undeformed zones is ragged, as crushing propagates by the progressive collapse of bands of cells that initiate at sites of "weaker" cells. In this case a small number of narrow zones of crushed cells have also appeared close to the upper end of the specimen. Neglecting the effect of these zones, the average strain in the lower part of the specimen remains at about 50%.

Image ③ corresponds to an average strain of 51%. The lower crushed zone has propagated further upward, but simultaneously an inclined band of crushed cells has developed close to the upper end of the specimen. This has left what appears in this view as a wedge of intact cells. This arrangement of highly deformed and essentially intact zones has induced local bending to the specimen with a concave edge on the right and a convex one on the left. This indicates that at this stage the deformation of the specimen is no longer axisymmetric.

Summarizing, the images confirm that, like low-density open-cell foams, compression leads to localization in the form of crushed bands of cells. Crushing subsequently propagates by band broadening with the stress remaining nearly unchanged and highly deformed and essentially undeformed domains coexisting. Similar conclusions have been reported in Chai et al. (2020), who used a synchrotron to follow the evolution of localized crushing of polymethacrylimide closed-cell foams with relative densities of 4.3% and 6.2% under axial compression (see also Tang et al., 2022). The more powerful and higher resolution X-ray source provided higher resolution images but for samples with fewer number of cells across the diameter – 4–6. Collectively these characteristics place the crushing behavior of low-density closed-cell foams in the category of propagating instabilities.

4.3 Summary of Triaxial Experiments

Returning to triaxial loading, compression experiments on foam specimens were performed for pressures ranging from 0 to 8.12 bar (0–118 psi), and the results are presented in summary form here. Each specimen was compressed until a well-defined stress plateau was established (typically to $d/H \sim 0.15$). Some specimens developed excessive bending during compression and were repeated. The nominal stress-shortening responses for eight of the experiments are plotted in Fig. 4.4, and the main material parameters of interest extracted from the responses are listed in Table 4.1. All responses exhibit a stiff initial branch that terminates in a stress maximum during which deformation is uniform. The stress maximum is a limit load instability that represents the

initiation of localized deformation. With the load in most cases dropping sharply, localization evolves into a band of crushed cells that covers the whole cross section. The band is typically located in the central third of the height. Once the band is fully developed the response traces a stress plateau during which it propagates axially.

The elastic moduli, E, calculated from the initial part of each response, exhibit a small decreasing trend with pressure, but because of scatter in the data a more quantitative conclusion is not supported. However, all values measured are well below the nominal pure compression modulus of the manufacturer of 125–135 MPa. The modulus is based on measured changes in height made by the laser extensometer on one side of the cylindrical specimen. Small misalignments and other imperfections can cause some bending to the cylindrical specimen, which can contribute to the observed scatter.

At higher stress levels the stable branch became nonlinear at all pressure levels and terminated in a limit load designated as the initiation stress, S_I (see Table 4.1). This is followed by the stress dropping down to the extended stress plateau. The drop varies in amplitude and in some experiments was masked, most likely because of imperfections. The initiation stress is seen in Fig. 4.5 to exhibit a clear decreasing trend with pressure. Scatter in the data is primarily caused first by small imperfections in the microstructure of the foam specimens and second by small variations in the tightening of the four bolts that can contribute to slightly eccentric loading. The parameters of the linear fit of the data are listed below Table 4.1. (Compare with similar plot from numerical triaxial results for open-cell foams in Yang and Kyriakides, 2020b.)

During the band propagation phase of the crushing, the stress traces a plateau. The value of the propagation stress, S_P, is determined from the section of the plateau with the smallest variation. These plateau regions vary in strain extent, and the measured propagation stress can vary on the order of 10 kPa (1 psi) based on the specific extent chosen. The propagation stress plotted against pressure included in Fig. 4.5 follows a decreasing trend with pressure that is somewhat steeper than that of S_I (parameters of linear fit listed below Table 4.1). Fig. 4.6 shows the extent of localization at the end of the experiments at pressure levels of {4.52, 6.17, 6.82, 8.12} bar (specimens unloaded and rubber membrane removed). Localization has evolved into a band that covers the full cross section for all four cases. The bands are somewhat ragged but nearly axisymmetric. The crushed material inside the bands has undergone lateral contraction, forming a groove on the surface of the cylinder the depth of which increases with pressure.

4.3.1 Pressure-Dominated Collapse

Lateral contraction is most significant for the 8.12 bar specimen, forming a neck-like shape that extends over the whole height of the specimen. It is worth noting that in this case the response, shown separately in Fig. 4.7a, exhibits a larger initial drop in pressure while steady-state axial propagation of a band and the associated stress plateau do not materialize. The evolution of localization during this experiment is illustrated through a sequence of photographic images taken throughout the experiment in Fig. 4.7b. Here also localization initiates near mid-height but starting from image ② at approximately the local minimum in the response, it takes the form of a diffuse neck that

affects most of the specimen. As compression progresses, the neck deepens with the narrowest section near mid-height developing “wrinkles,” conceivably due to non-uniform radial localization, best observed in the postmortem image in Fig. 4.6. The excessive deformation in this zone is in turn responsible for the twisted wrinkles developed in the elastic membrane covering the specimen. At this and presumably higher pressure levels, steady-steady axial propagation is no longer supported; the pressure plays a more dominant role and imposes a different localization behavior.

Motivated by the behavior of specimen FM8 compressed at a pressure of 8.12 bar, the response of the foam under pure external pressure was investigated. Three specimens were tested under pressure-only loading in the same test setup. The pressure was increased at intervals of about 0.7 bar (10 psi) up to a pressure of 7.6 bar (110 psi) and at smaller increments for higher pressures. The loading was briefly paused after each increment until the pressure stabilized. The induced overall axial displacement was again recorded by the laser extensometer, and images of the full deforming specimen were recorded at 4 s intervals. The behavior is demonstrated in Fig. 4.8, where the relevant part of the pressure-axial displacement response is shown expanded together with six overall images of the specimen that illustrate the associated instability. In image ① the specimen is deformed uniformly. As the pressure increases, the response becomes increasingly nonlinear, and image ② shows the first signs of localized contraction concentrated at mid-height. With the supply of air halted, the pressure reaches a maximum value between stations ② and ③ and then starts to gradually drop. In images ③ to ⑥ the specimen

develops diffuse necking and beyond station ⑥ the pressure is gradually released, with the specimen permanently crushed.

The same behavior was observed in the other two pure pressure experiments, with the onset of instability occurring at pressures between 8.83 and 9.22 bar (128.0–133.7 psi). The photograph in Fig. 4.8c shows a postmortem image of a specimen from one of the other two tests. In this test the specimen was allowed to deform more extensively before the pressure was removed, and the specimen shows severe necking with wrinkles superimposed in the most deformed section. Broadly, this behavior is similar to that of the specimen from FM8 in Fig. 4.7, which was compressed axially under displacement control at 8.12 bar external pressure. The three pure pressure tests confirm that the foam crushes with two different mechanisms that depend on the level of applied pressure.

In summary, axial compression at different pressure levels causes a limit load instability that induces localized deformation in the form of cell crushing. Subsequently, the localization spreads axially with the stress remaining nearly unchanged. The crushing zone also develops radial contraction that increases with pressure. Both the initiation and propagation stresses decrease nearly linearly with pressure. At higher levels of pressure, steady-state axial propagation of localized deformation is replaced by a more axially diffuse mode of localization.

4.4 Fitting a Drucker-Prager Yield Function

To characterize the yield response of the Divinycell foam, a Drucker-Prager (1952) yield surface was fitted to the triaxial crushing data. Neglecting the anisotropy in

the microstructure reported in Section 2.2 (see also Steeves and Fleck, 2004), the yield function is expressed as

$$f = [3J_2 + \alpha^2 (I_1/3)^2]^{1/2} = [1 + (\alpha/3)^2]^{1/2} \sigma_o, \tag{4.1}$$

where I_1 is the first invariant of the stress tensor, J_2 is the second invariant of its deviator, and σ_o is the yield stress under uniaxial compression (e.g., Deshpande and Fleck, 2000; Gioux et al., 2000; Ruan et al., 2007; Shafiq et al., 2015a; Yang and Kyriakides, 2020a, 2020b). A derivation of the least squares-optimal material parameter α minimizing the algebraic distance of the data from the ellipse of the yield surface is given in Appendix D.

To fit the yield surface to the crushing data, a yield stress must be selected for each σ - d/H response. A common method of determining the yield stress from these crushing responses is the strain offset method, in which a line with a slope corresponding to the stiffness derived from a small subsample in the linear region of deformation is offset in strain by a constant, for metals commonly 0.2%. The yield stress is then determined by the stress at which the experimental crushing response intersects the offset line.

To better fit the yield stresses collected from the triaxial crushing experiments to the Drucker-Prager surface, rather than simply selecting a strain offset, its value was optimized based on a numerical analysis. A set of four hundred strain offsets ranging from 0.02% to 0.4% was tested, at each strain offset evaluating the least squares optimal fit parameter α. The yield stress in all cases was determined with the strain offset

chosen. This was also applied to the uniaxial experiment FM5 used to determine the uniaxial yield stress σ_o. The quality of the fit for each tested strain offset is evaluated by the cost J as shown in Eq. (D.4) in Appendix D.

Fig. 4.9 shows the cost at each strain offset normalized by the uniaxial yield stress σ_o. The variation of fit quality with increasing strain offset is such that there is a minimum value representing the best possible least squares fit of the data to the yield surface, and the fit becomes poorer with small or large strain offset. The minimum cost strain offset is 0.15%. This results in yield stress values that are below the initiation stresses recorded in the experiments.

The yield stress, $\sigma_o(P)$, was therefore determined from each triaxial response using a 0.15% strain offset (see Table 1). For uniaxial compression, the yield stress is found to be σ_o = 1.303 MPa (189 psi), which compares with 1.346 MPa reported by Shafiq et al. (2015) (average of three values based on a 0.2% strain offset).

The optimized yield surface is plotted as $I_1/3\sigma_o$ against $\sqrt{3J_2}/\sigma_o$ in Fig. 4.10. Included is a best fit of the data ensuring that it passes through the uniaxial compression yield stress. The resultant value for a is 0.889, and the intercept on the ordinate is 1.048. In view of the observed switch in behavior at higher pressure levels, the yield function is truncated as shown in the figure.

It was not possible to record the yield stresses for the pure pressure experiments. The pressures at which these specimens failed are included on the abscissa with different

symbols. The results are clearly inconsistent with the triaxial yield stresses recorded in different experiments, and they provide additional evidence that the failure mechanism under pure pressure is different from that seen under lower pressure triaxial loading. This distinct failure mechanism warrants further investigation.

Ex. No.	P bar (psi)	E MPa (ksi)	σ_I MPa (psi)	σ_P MPa (psi)	σ_o MPa (psi)
FM5	0	92.40 (13.40)	1.509 (218.8)	1.408 (204.2)	1.303 (189.0)
FM6	0	81.34 (11.79)	1.400 (203.0)	1.190 (2172.6)	1.269 (184.0)
FM14	1.68 (24.4)	101.9 (14.78)	1.494 (216.6)	1.328 (192.5)	1.010 (146.5)
FM12	2.48 (36)	85.09 (12.34)	1.420 (205.9)	1.131 (164.0)	1.298 (188.3)
FM10	4.52 (65.5)	71.39 (10.35)	1.218 (176.6)	1.058 (153.4)	1.093 (158.5)
FM9	5.50 (79.7)	90.63 (13.14)	1.108 (160.6)	0.987 (143.1)	1.092 (158.4)
FM11	6.17 (89.4)	79.55 (11.53)	1.136 (164.7)	0.827 (119.9)	1.081 (156.7)
FM7	6.82 (98.9)	78.67 (11.41)	1.107 (160.6)	0.757 (109.7)	1.025 (148.6)
FM8	8.12 (117.8)	74.28 (10.77)	0.882 (127.9)	0.484* (70.12)	0.880 (127.5)

* No plateau

Linear fits: $\sigma_I = 231 - 0.7872P$ psi; $\sigma_P = 205 - 0.8794P$ psi

Table 4.1: The mechanical properties of Divinycell H100 foam at different pressure levels as determined from triaxial experiments.

(a)

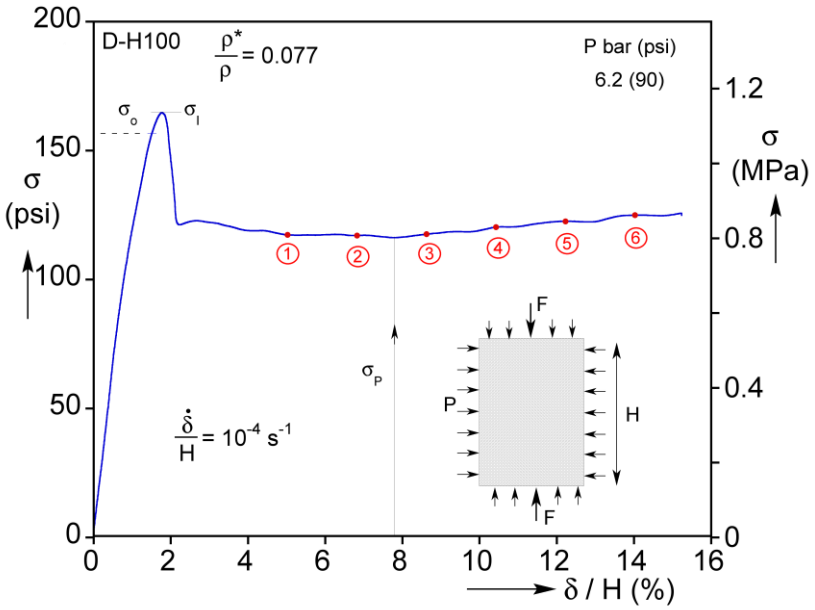

(b)

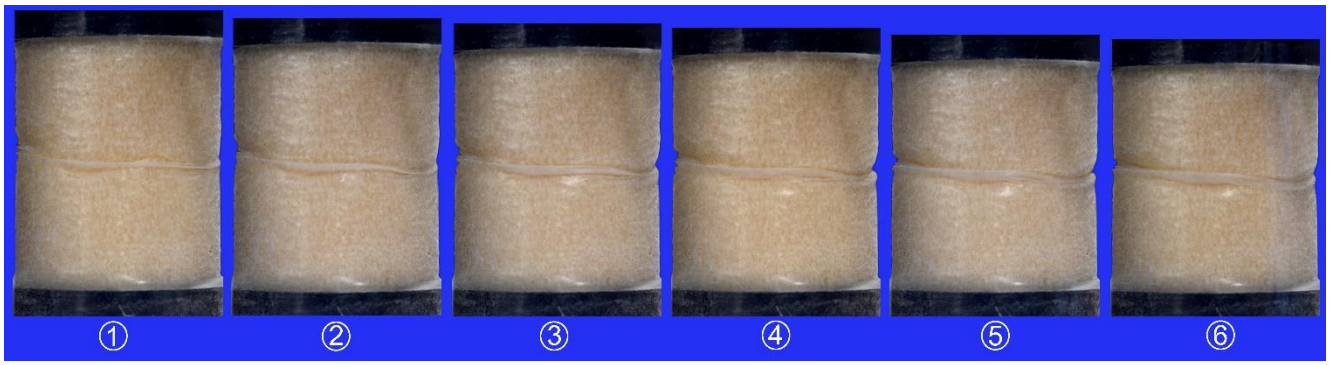

(c)

Figure 4.1: Summary of results of specimen FM11 compressed under 6.2 bar external pressure. (a) Axial stress-shortening response. (b) Sequence of photographic images showing the evolution of localization; correspond to numbered sites on the response in (a). (c) Postmortem image of the test specimen.

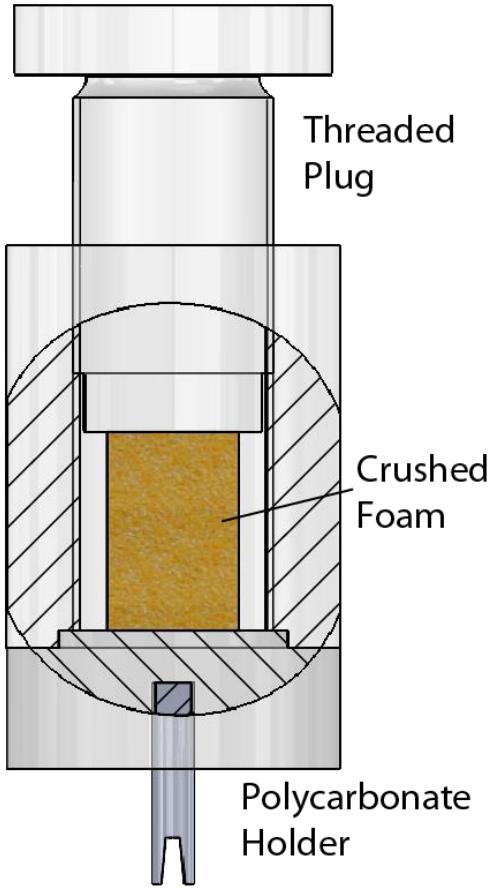

Figure 4.2: The threaded plug design used to hold and maintain the strain of a crushed foam specimen in the μCT 80 computer tomography scanner.

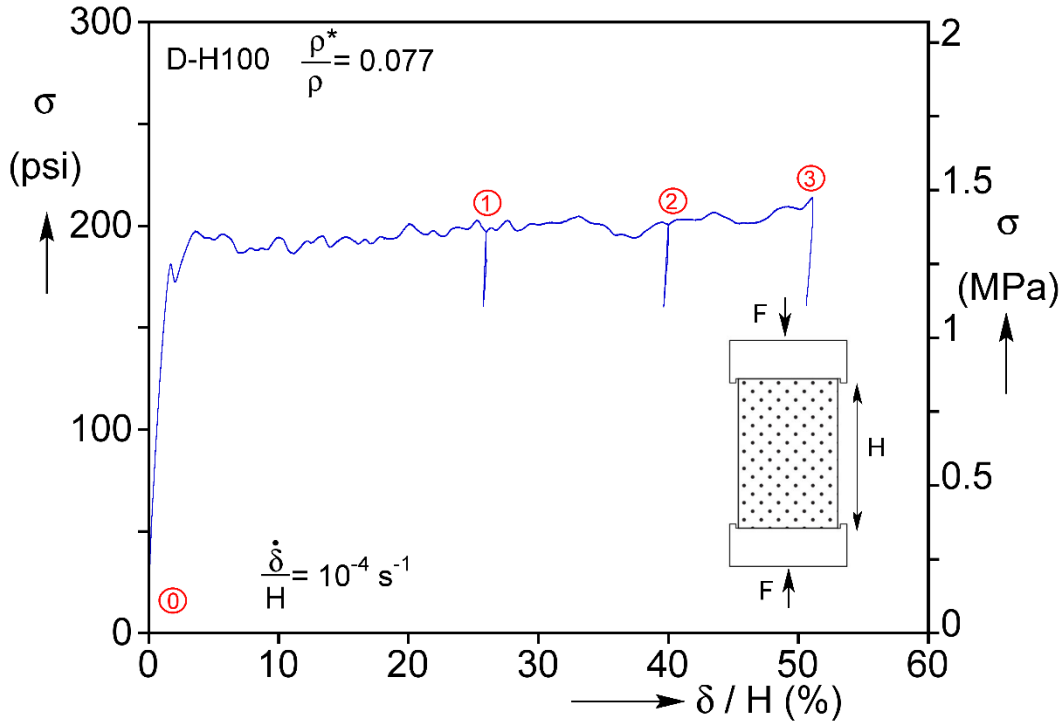

(a)

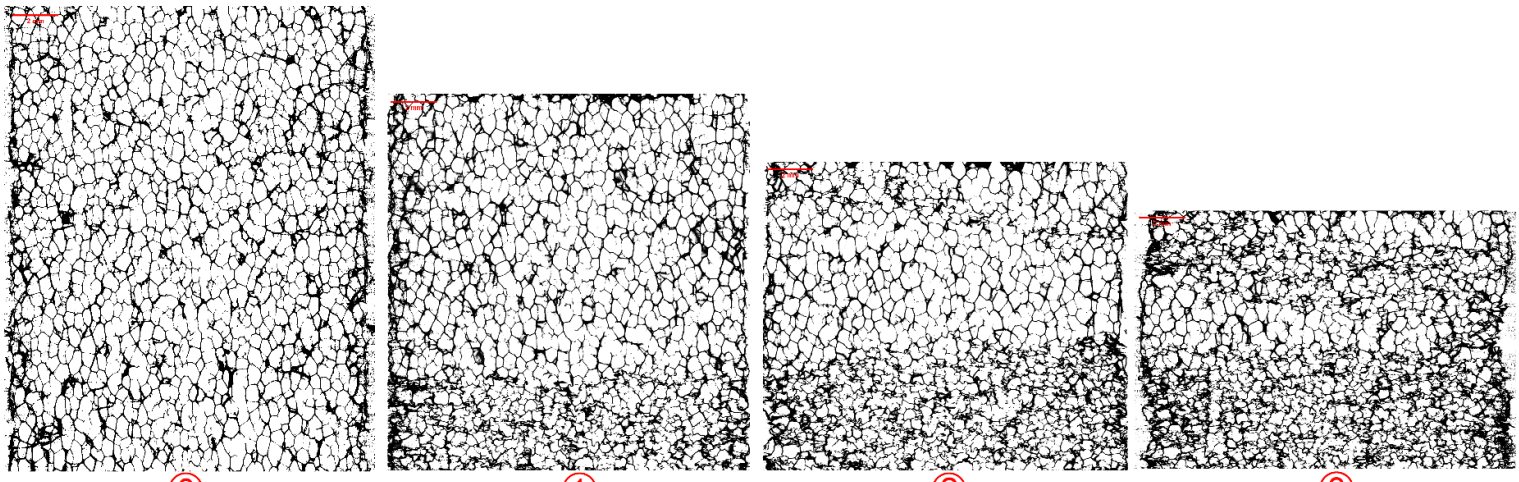

(b)

Figure 4.3: (a) Stress-shortening response, and (b) X-ray tomography images showing evolution of localized crushing zones at different stages of compression displacement (images show 30× 40 cell section).

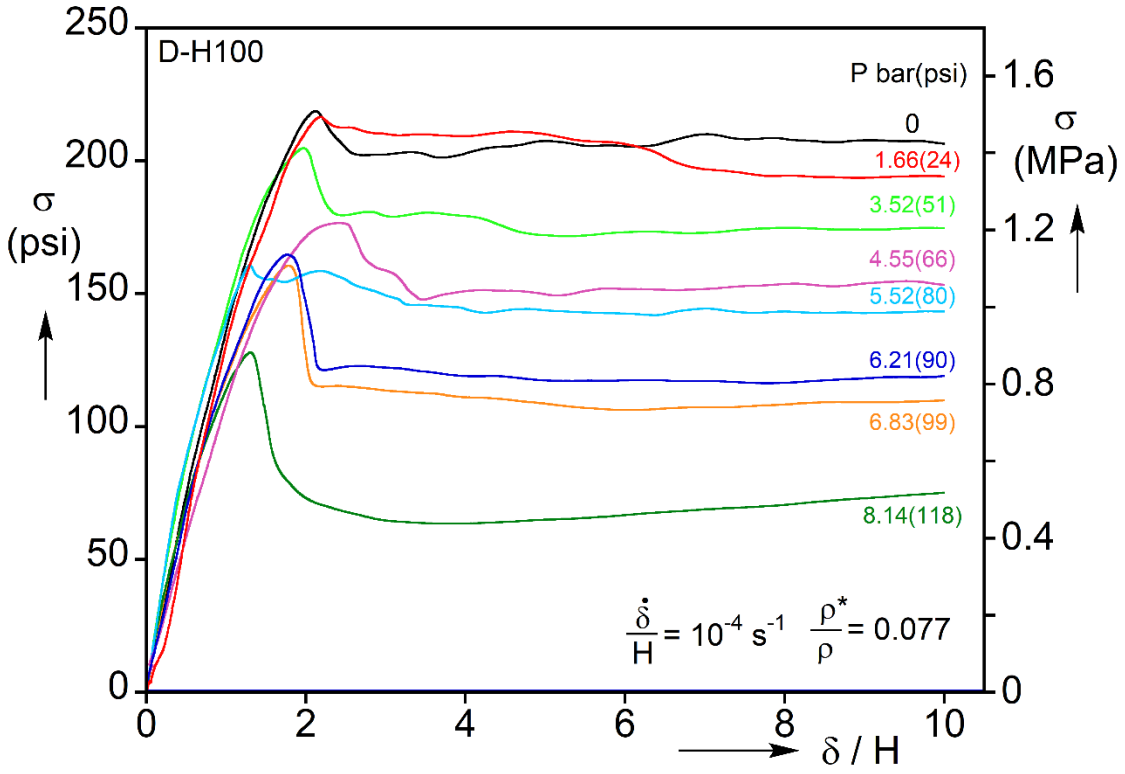

Figure 4.4: Axial stress-shortening responses recorded in triaxial experiments on D-H100 specimens tested at different pressure levels.

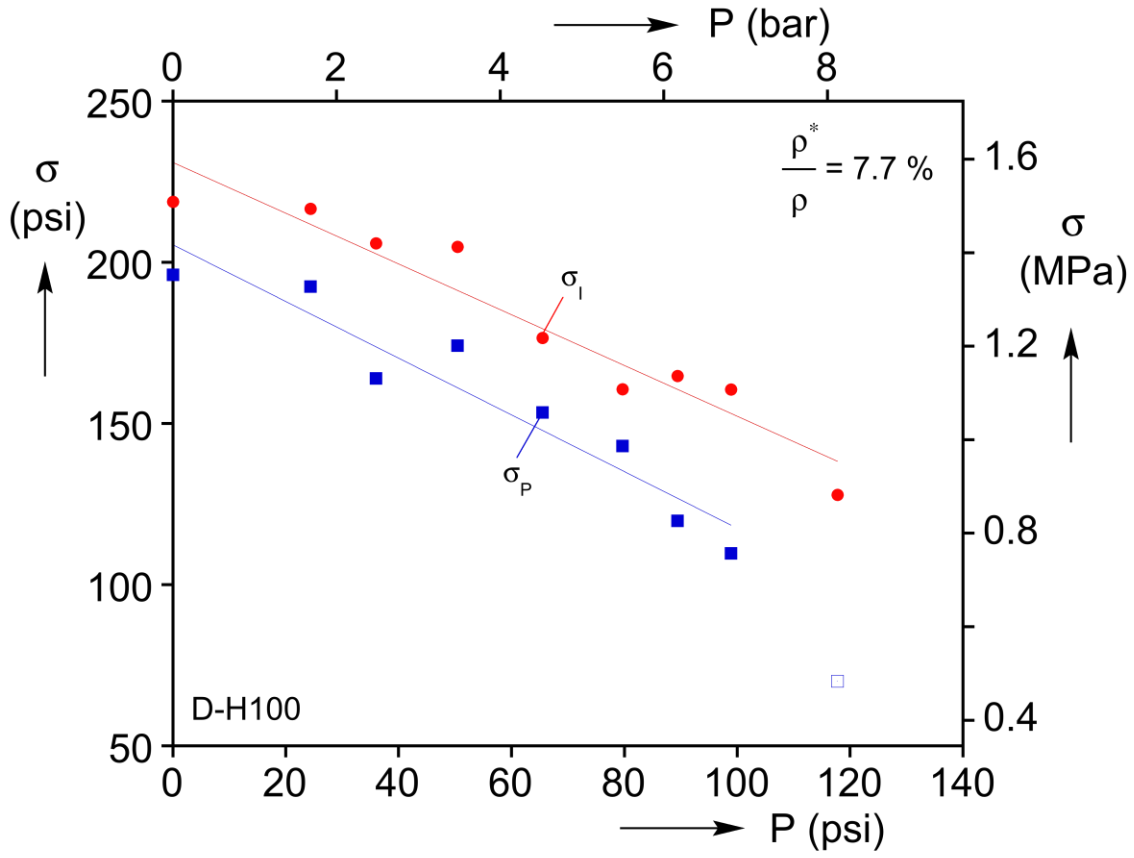

Figure 4.5: Measured axial stress at the initiation of localization (σ_I) and at the stress plateau (σ_P).

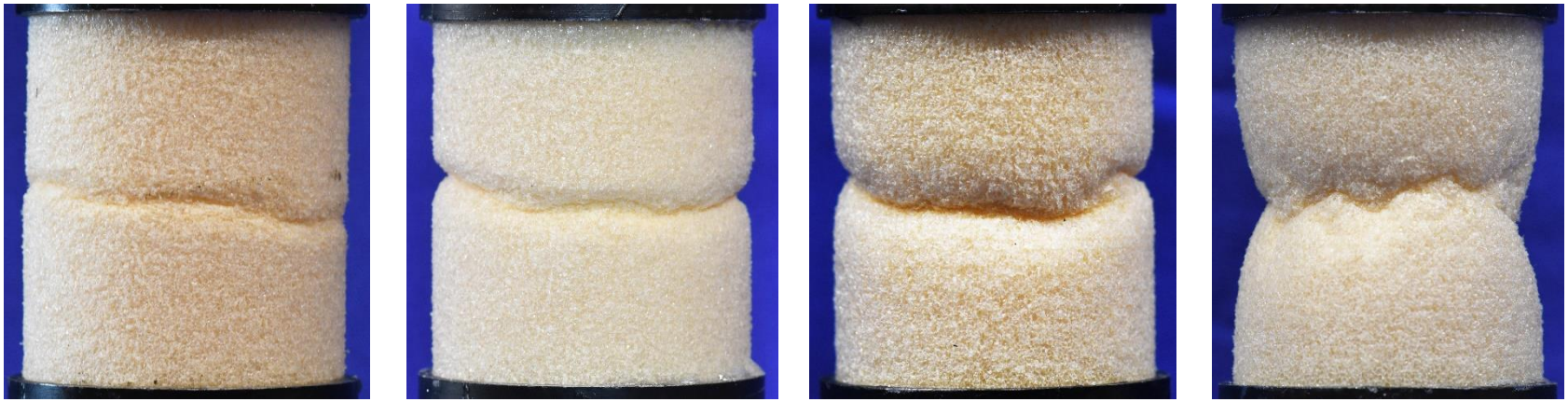

FM10-4.52 FM11-6.17 FM7-6.82 FM8-8.12

Figure 4.6: Postmortem foam specimens tested at progressively higher pressure. The localization zone contacts and broadens more as pressure increases.

(a)

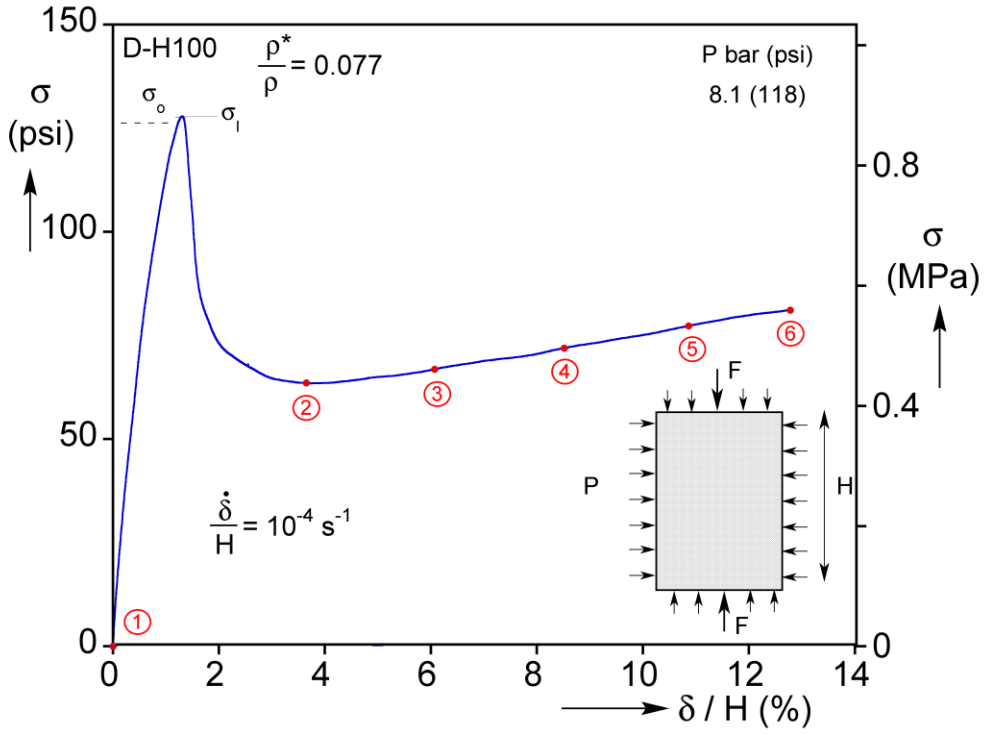

(b)

Figure 4.7: Summary of results of specimen FM8 compressed under 8.12 bar external pressure. (a) Axial stress-shortening response. (b) Sequence of photographic images showing the evolution of localization; correspond to numbered sites on the response in (a).

(a)

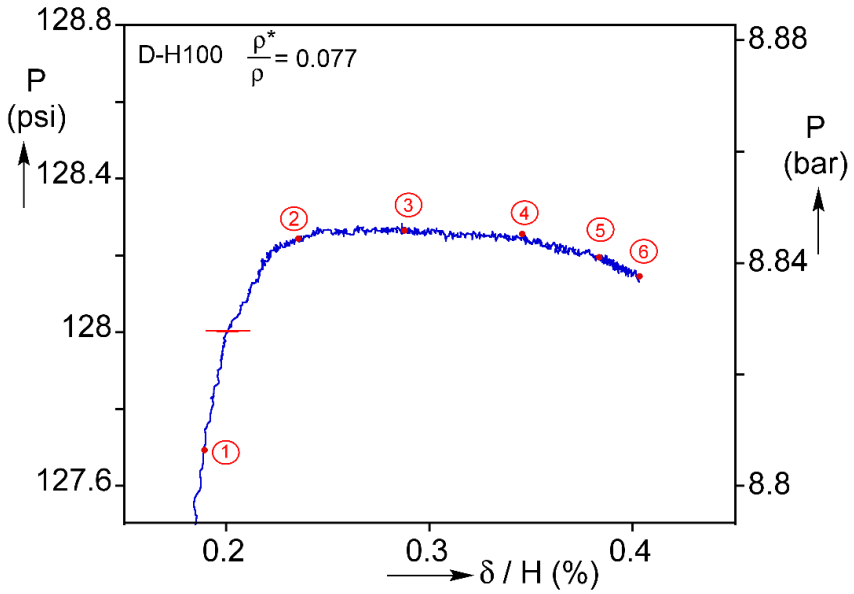

(b)

(c)

Figure 4.8: Results from a pure pressure experiment: (a) Expanded pressure-axial shortening response at the onset of lateral crushing. (b) Photographic images showing the specimen as it crushes. (c) Postmortem image of a test specimen crushed by external pressure.

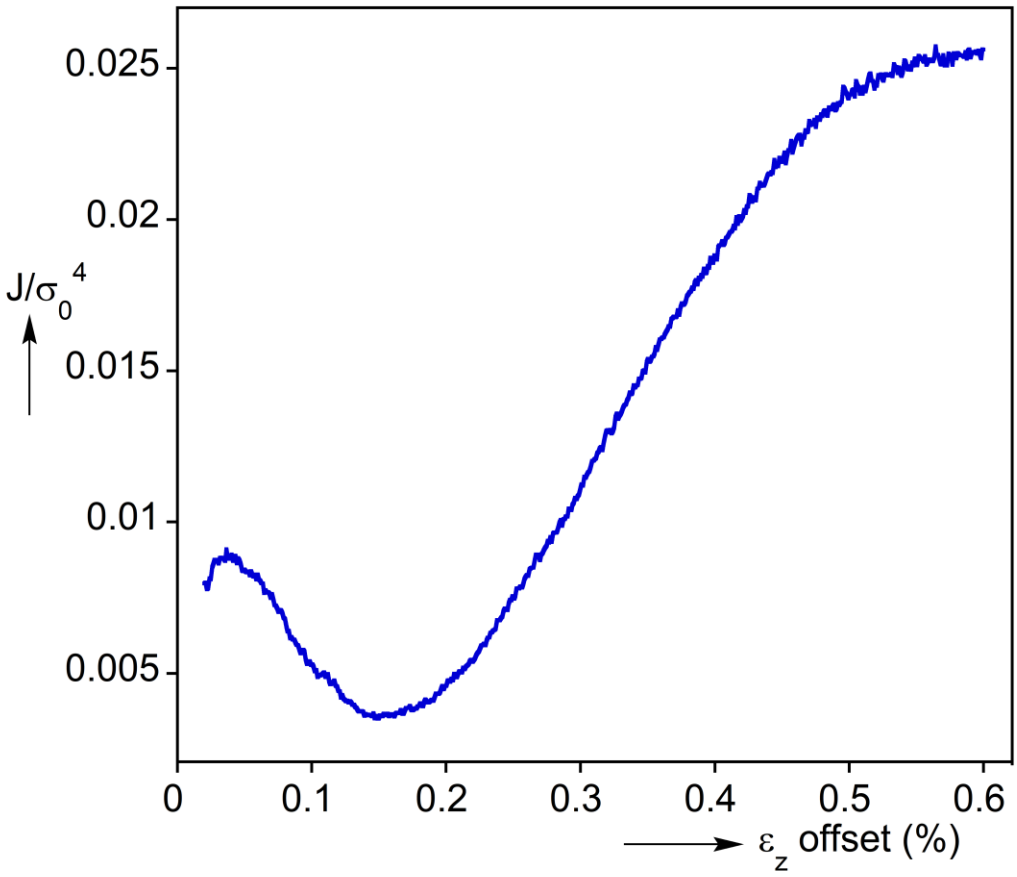

Figure 4.9: The cost J associated with the optimal Drucker-Prager yield surface fit parameter α as a function of the strain offset used to determine the yield stresses. The cost is normalized by the uniaxial yield stress s_o.

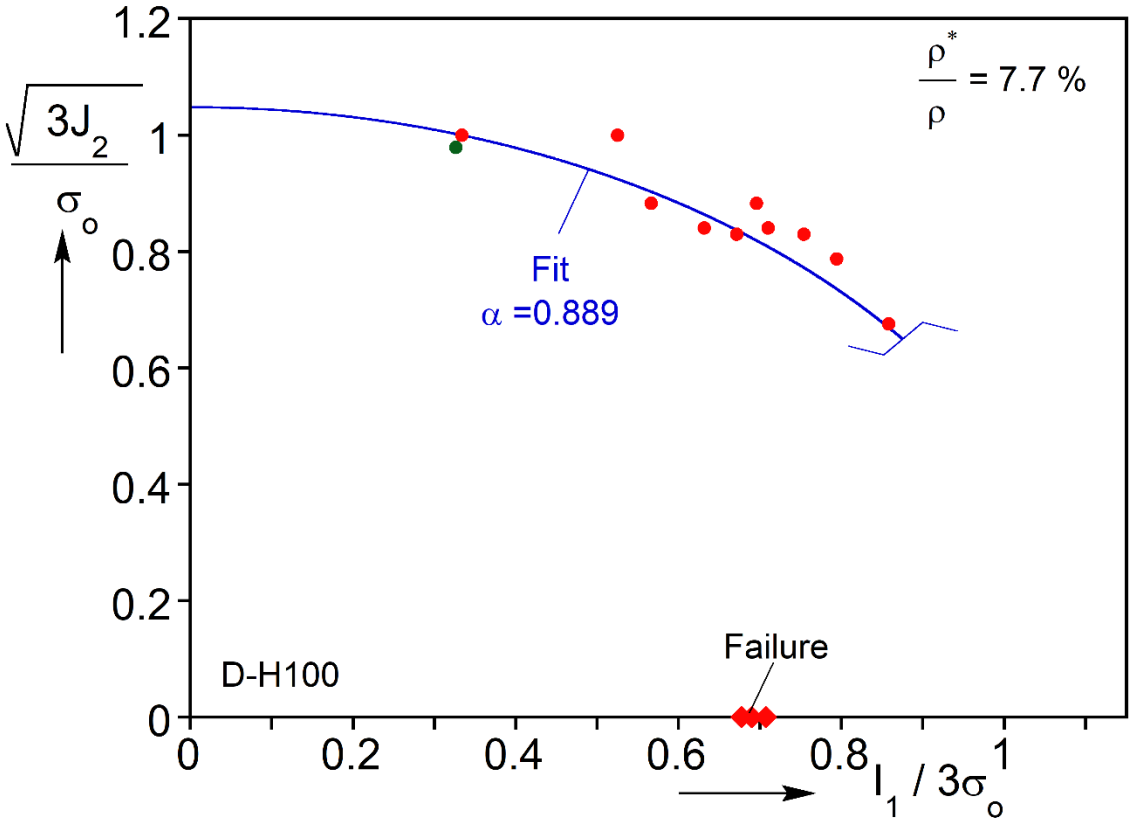

Figure 4.10: The Drucker-Prager initial yield surface calibrated to yield stresses from the triaxial D-H100 foam experiments. $s_o = 1.303$ MPa is the yield stress for pure compression.

Chapter 5: Conclusions

This study investigated the microstructure and deformation behavior of Divinycell H-100, a closed-cell polymeric foam with a relative density of 7.7%. The foam microstructure was probed in detail using a μCT 80 computed tomography scanner. A set of image analysis tools were used to identify cell boundaries and to analyze the cell size, face thickness, and anisotropy.

A custom-designed and built triaxial testing apparatus was used to investigate the deformation behavior of the D-H100 foam under various loading conditions. Cylindrical specimens (38× 50 mm) were axially crushed under constant external pressure at a slow displacement rate in a custom triaxial loading apparatus with a transparent containment vessel. The specimen shortening was recorded with a non-contact extensometer. The deformation, load, and pressure were continuously recorded using a DAQ system in a custom LabVIEW setup, while the overall deformation of the specimen was monitored photographically with a DSLR camera.

For a series of 11 axial crushing experiments, a compressible Drucker-Prager yield surface was fitted to the recorded data, demonstrating the foam's strong sensitivity to pressure. Three additional experiments with purely pressure loading and no axial loading were conducted to investigate an independent pressure-dominated collapse condition that appears above some critical pressure. A smaller foam cylinder with 30x40 cells was used to capture the evolution of crushing under axial compression at the microstructural level using micro computed tomography. These results firmly place the

deformation of the foam in the category of propagating instabilities. This is in conflict with the present state of the art (Dassault Systèmes, 2023) constitutive models that are based on the assumption that the foam deforms homogeneously (see also Deshpande and Fleck, 2000). The following additional conclusions can be drawn from the study:

Microstructure

- The scans of D-H100 using µCT 80 required additional processing for image analysis due to the low density of the foam, as some regions of the foam material are near the threshold of the background noise. After thresholding, the raw TIFF data produced by the µCT 80 scanner was treated with a watershed split algorithm to restore cell boundaries for accurate cell size and anisotropy measurement.
- Extra care must be taken in producing face thickness measurements, as many X-ray scanners do not have sufficiently small voxel size to resolve the small-scale structure of the foam faces.
- The cell sizes as measured by the Extended Particle Analyzer and the face thicknesses as measured by the Local Thickness algorithm are well modeled by lognormal distributions.
- The cells exhibit low polydispersity with a cell diameter relative deviation of 0.183. The mean cell size is 0.5 mm, and the mean wall thickness is 0.0348 mm. The cells are elongated along the rise direction, inducing an anisotropy of 1.4.
- The microstructure consists of interconnected irregular polyhedra with faces of near constant thickness and concentration of material near nodes that join four faces.

Triaxial Crushing Experiments

The typical axial force-displacement response under triaxial loading consists of an initial stiff branch where the foam deforms elastically. The stiff branch terminates into a load maximum beyond which deformation localizes into a horizontal axisymmetric band of crushed cells with parabolic side grooves. The band then propagates axially with the stress remaining nearly constant, characteristic of materials that exhibit propagating instabilities. The following additional observations can be made from the results:

- The crushing behavior outlined above was consistently observed for crushing experiments at pressures up to about 7 bar (102 psi), with the side grooves becoming deeper as the pressure increased. Pressure lowers both the stress maximum (initiation stress) and the plateau stress (propagation stress), with both exhibiting a linear decreasing trend with pressure.
- At higher pressures levels, lateral contraction in the form of a neck replaced the axial crushing, and the axial stress plateau did not materialize. The primarily lateral crushing is presumably a result of the reported anisotropy in the microstructure. This lateral contraction-dominant crushing was also observed in three pure pressure experiments, in which the specimens failed between 8.83 and 9.22 bar (128.0–133.7 psi). This mode of failure and the pressure at which it becomes dominant require further investigation.
- A strain offset of approximately 0.15% in determining the yield stress produced the highest quality fit to a Drucker-Prager yield function. The pressure-dominated yield

does not fit to the Drucker-Prager yield surface and must be independently investigated.

- In the analysis of the progressively deforming smaller specimen, scans at different stages of compression showed nearly horizontal zones of crushed shells with a strain of about 50% to coexist with essentially undeformed cells. As the crushing progresses, the zones broaden axially while the stress traces a plateau that is at about the same level as that recorded in the larger specimens – results consistent with those in Chen et al., 2020, for a different polymeric closed-cell foam.
- The overall behavior of this closed-cell foam is similar to that reported for crushing of open-cell foams under triaxial loading performed numerically on microstructurally accurate open-cell foams (Yang and Kyriakides, 2020b).

Appendix A

ANISTROPIC KELVIN CELL MODEL WITH EXPANDING SPHERES

The regular Kelvin cell model can be extended to include the effect of a stretched unit cell accounting for anisotropy; here it is also extended to account for concentration of the foam material at nodes corresponding to the junction of four adjacent Kelvin cells through the addition of expanding spheres at these vertices. A simple formula for the volume of the solid material in the Kelvin cell is developed by accounting for the solid volume in the two horizontal square planes, four vertical square planes and six vertical hexagonal planes, as well as the volume concentrated in the spheres. The plane volumes must have the common volume of the plane and the spheres removed to avoid double accounting for this intersecting volume:

$$V_s = 2\left(\frac{t}{2}A_{\text{sq, H}} - V_{\text{intersect,1}}\right) + 4\left(\frac{t}{2}A_{\text{sq, V}} - V_{\text{intersect,2}}\right) + 8\left(\frac{t}{2}A_{\text{hex}} - V_{\text{intersect,3}}\right) + \frac{V_{\text{spheres}}}{4}. \quad \text{(A.1)}$$

The areas of the faces are multiplied by the face thickness $\frac{t}{2}$, accounting for the fact that each face belongs to two Kelvin cells. The areas of the horizontal square, vertical square, and hexagonal faces are respectively given by,

$$A_{\text{sq, H}} = b^2,\ A_{\text{sq, V}} = L^2,\ A_{\text{hex}} = 2bL\sin\phi + 2L^2\sin\phi\cos\phi\ . \quad \text{(A.2)}$$

The intersecting volume of the square and hexagonal faces with the spheres centered at the vertices can be expressed through a spherical integration of independent coordinates:

$$V_{\text{intersect}} = \iiint \rho \sin\varphi d\rho d\theta d\varphi = (\cos\varphi_1 - \cos\varphi_2)(\theta_2 - \theta_1)\left(\frac{1}{3}R^3\right) = (\theta_2 - \theta_1)\left(\frac{1}{6}tR^2\right). \quad \text{(A.3)}$$

The angle subtended by the squares is $\theta_2 - \theta_1 = \pi/2$ and by the hexagons, $\theta_2 - \theta_1 = 2\pi/3$. The intersecting volumes are therefore given by,

$$V_{\text{intersect},1} = V_{\text{intersect},2} = \frac{\pi}{12}tR^2,\ V_{\text{intersect},3} = \frac{\pi}{9}tR^2. \quad \text{(A.4)}$$

Simplifying Eq. (A.2) for the expressions in (A.3) and (A.4) leads to Eq. (2.7). It should also be noted that the angle θ as shown in Fig. 2.9 is a nonlinear function of the anisotropy parameter λ . Defining $\tan\alpha = \lambda$, this relationship is given by,

$$2\sin\theta = \tan\alpha\left(\cos\theta + \cos\alpha\right). \quad \text{(A.5)}$$

Eq. (A.5) must be solved numerically but can be easily solved with an initial guess $\theta = \pi/2$. Further, the angle ϕ is a simple function of the angle θ because of the constraints imposed by the geometry of the Kelvin cell:

$$\sin\phi = \sqrt{1 - \frac{1}{2}\cos^2\theta}. \quad \text{(A.6)}$$

Appendix B

PLANE STRAIN DEFORMATION AND LOADING OF THE ACRYLIC PRESSURE VESSEL

To ensure the acrylic pressure vessel could function within the constraints of the triaxial cell design and the loading it was subjected to, a simple theoretical model was established using an Airy stress function and assuming plane strain conditions. This analysis relies on a single equilibrium equation for the stress in cylindrical coordinates:

$$\frac{\partial \sigma_r}{\partial r} + \frac{1}{r}\left(\sigma_r - \sigma_\theta\right) = 0 . \tag{B.1}$$

The two boundary conditions apply to the radial stress at the inner and outer boundaries of the pressure vessel, and the outer pressure is assumed to be much smaller than the inner pressure:

$$\sigma_r\left(r = r_o\right) = 0 , \tag{B.2A}$$

$$\sigma_r\left(r = r_i\right) = -p , \tag{B.2B}$$

The simplest Airy stress function satisfying this equilibrium equation and the boundary conditions is given by,

$$\phi = a_0 + a_1 \log r + a_2 r^2 . \tag{B.3}$$

The Airy stress function is related to the nonzero stresses as,

$$\sigma_r = \frac{1}{r}\frac{\partial \phi}{\partial r} = \frac{a_1}{r^2} + 2a_2 , \tag{B.4A}$$

$$\sigma_\theta = \frac{\partial^2 \phi}{\partial r^2} = -\frac{a_1}{r^2} + 2a_2 , \tag{B.4B}$$

$$\sigma_z = \nu\left(\sigma_r + \sigma_\theta\right) = 4\nu a_2 . \tag{B.4C}$$

Applying the boundary conditions, the stresses are given by,

$$\sigma_r = \frac{r_i^2 p}{r_o^2 - r_i^2}\left(1 - \frac{r_o^2}{r^2}\right), \tag{B.5A}$$

$$\sigma_\theta = \frac{r_i^2 p}{r_o^2 - r_i^2}\left(1 + \frac{r_o^2}{r^2}\right), \tag{B.5B}$$

$$\sigma_z = \frac{2\nu r_i^2 p}{r_o^2 - r_i^2} . \tag{B.5C}$$

Applying the von Mises yield condition at the inner surface of the thick-walled pressure vessel where the stress is maximized, the pressure at yield is then a simple function of the yield stress of the acrylic material:

$$p_y = \frac{r_o^2 - r_i^2}{\sqrt{3r_o^4 + \left(1-2\nu\right)^2 r_i^4}}\sigma_y . \tag{B.6}$$

Further, the stress functions can be transformed to a cylindrical strain in the hoop direction assuming linear elasticity. Exploiting the cylindrical symmetry, the hoop strain is a simple function of the radial displacement:

$$\varepsilon_\theta = \frac{u_r}{r} = \frac{p r_i^2\left(r_o^2 + \left(1-2\nu\right)r^2\right)\left(1+\nu\right)}{E r^2\left(r_o^2 - r_i^2\right)} . \tag{B.7}$$

The radial displacement at the outer boundary of the pressure vessel is therefore given by,

$$u_r\left(r_o\right)=\frac{2pr_i^2r_o\left(1-\nu\right)\left(1+\nu\right)}{E\left(r_o^{\,2}-r_i^2\right)}. \tag{B.8}$$

Appendix C

A WHEATSTONE BRIDGE COMPENSATING FOR TEMPERATURE AND BENDING

It is essential to the design of the described triaxial experiments that only the axial loading of the brass load cell is recorded in the data acquisition system. To fulfill this requirement, the strain gages were placed in a specific arrangement designed to automatically cancel the loading caused by expansion or contraction by temperature changes and bending induced by axial loading. The three strain loads at strain gage i due to axial loading, ε_a, bending, ε_b, and temperature change ε_T are considered independently through superposition:

$$\varepsilon_i = \varepsilon_{a_i} + \varepsilon_{b_i} + \varepsilon_{T_i}. \tag{C.1}$$

The Wheatstone bridge utilizes four strain gages such that the voltage signals from two strain gages are subtracted from the voltage signals of the other two. This relationship is given in terms of the gage factor G and stiffness E:

$$\frac{\Delta V}{E} = \frac{G}{4}\left[\varepsilon_1 - \varepsilon_2 + \varepsilon_3 - \varepsilon_4\right]. \tag{C.2}$$

Placing two strain gages with the long edge along the hoop direction and two with the long edge along the axial direction as shown in Fig. 3.3, the strain terms for the four strain gages are given by,

$$\frac{\Delta V}{E} = \frac{G}{4}\left[\left(\varepsilon_a + \varepsilon_{b_x} + \varepsilon_T\right) - \left(-\nu\varepsilon_a + \varepsilon_{b_y} + \varepsilon_T\right) + \left(\varepsilon_a - \varepsilon_{b_x} + \varepsilon_T\right) - \left(-\nu\varepsilon_a - \varepsilon_{b_y} + \varepsilon_T\right)\right]. \quad \text{(C.3)}$$

Simplifying the expression in Eq. (C.3), the measured voltage change across the bridge is thus given by the gage factor G, the Poisson ratio of the brass, and the axial strain ε_a:

$$\frac{\Delta V}{E} = G\frac{1+\nu}{2}\varepsilon_a . \quad \text{(C.4)}$$

Appendix D

LEAST SQUARES FITTING A DRUCKER-PRAGER YIELD SURFACE

The Drucker-Prager yield surface is defined in terms of the first invariant of the stress tensor, I_1, and the second invariant of the deviatoric stress tensor, J_2. These are expressed in terms of the mean stress σ_m and the effective stress σ_e, which are themselves functions of the axial force on the cylindrical specimen, σ_0, and the isostatic pressure, p:

$$\sigma_m = -\left(p + \frac{\sigma_0}{3} \right) = \frac{I_1}{3}, \tag{D.1A}$$

$$\sigma_e = \sigma_0 = \sqrt{3J_2}\,. \tag{D.1B}$$

The yield surface is then defined in terms of the mean and effective stress as,

$$\sigma_e{}^2 = -\alpha^2 \sigma_m{}^2 + \left(1 + \left(\frac{\alpha}{3} \right)^2 \right) \sigma_0{}^2 . \tag{D.2}$$

To establish a cost to minimize when fitting the yield surface to a given set of data (σ_e, σ_m), it is simple to use the algebraic distance from the ellipse of the yield surface:

$$F(\sigma_e, \sigma_m) = \sigma_e{}^2 + \alpha^2 \left(\sigma_m{}^2 - \frac{\sigma_0{}^2}{9} \right) - \sigma_0{}^2 . \tag{D.3}$$

The uniaxial yield stress $\sigma_0 = Y$ was set as the yield stress determined by a 0.15% strain offset for a single high quality uniaxial crushing experiment. This means that the only parameter to fit with the least squares technique is α^2. To perform this fit, minimize the summed-squared algebraic distance J from the ellipse for all points (σ_e, σ_m):

$$J = \frac{1}{N}\sum_{i=1}^{N} F^2(\sigma_{e,i}, \sigma_{m,i}) = \frac{1}{N}\sum_{i=1}^{N}\left({\sigma_{e,i}}^2 + \alpha^2\left({\sigma_{m,i}}^2 - \frac{{\sigma_0}^2}{9}\right) - {\sigma_0}^2\right)^2 . \quad \text{(D.4)}$$

To find the least squares-optimal α^2, apply the first order necessary condition:

$$\frac{\partial}{\partial \alpha^2}\sum_{i=1}^{N} F^2(\sigma_{e,i}, \sigma_{m,i}) = \sum_{i=1}^{N} 2\left({\sigma_{e,i}}^2 + \alpha^2\left({\sigma_{m,i}}^2 - \frac{{\sigma_0}^2}{9}\right) - {\sigma_0}^2\right)\left({\sigma_{m,i}}^2 - \frac{{\sigma_0}^2}{9}\right) = 0 . \quad \text{(D.5)}$$

The function has only a single solution, at which the summed-squared algebraic distance J is minimized:

$$\alpha^2 = \frac{\sum_{i=1}^{N}\left({\sigma_0}^2 - {\sigma_{e,i}}^2\right)\left({\sigma_{m,i}}^2 - \frac{{\sigma_0}^2}{9}\right)}{\sum_{i=1}^{N}\left({\sigma_{m,i}}^2 - \frac{{\sigma_0}^2}{9}\right)} . \quad \text{(D.6)}$$

References

Ashby, M.F., Evans, A., Fleck, N.A., Gibson, L.J., Hutchinson, J.W. and Wadley, H.N.G., (2000). *Metal Foams: A Design Guide*. Butterworth-Heinemann.

Beckmann, C., Hohe, J. (2016). A probabilistic constitutive model for closed-cell foams. *Mech. Mat.* **96**, 96-105. https://doi.org/10.1016/j.mechmat.2016.01.016

Chai, H.W., Xie, Z.L., Xiao, X.H., Xie, H.L., Huang, J.Y., Luo, S.N. (2020). Microstructural characterization and constitutive modeling of deformation of closed-cell foams based on in situ x-ray tomography. *Int'l J. Plast.* **131**, 102730. https://doi.org/10.1016/j.ijplas.2020.102730

Chen, Y., Das, R., Battley, M. (2015). Effects of cell size and cell wall thickness variations on the stiffness of closed-cell foams. *Int'l J. Solids Struct*. **52**, 150-164. https://doi.org/10.1016/j.ijsolstr.2014.09.022

Daphalapurkar, N.P., Hanan, J.C., Phelps, N.B., Bale, H., Lu, H. (2008). Tomography and simulation of microstructure evolution of a closed-cell polymer foam in compression. *Mech. Adv. Mater. Struct*. **15**, 594-611. https://doi.org/10.1080/15376490802470523

Dassault Systèmes (2023). *ABAQUS Theory Manual*. Dassault Systèmes Simulia Corp.

Deshpande, V.S., Fleck, N.A. (2000). Isotropic constitutive models for metallic foams. *J. Mecha. Phys. Solids* **48**, 1253-1283. https://doi.org/10.1016/S0022-5096(99)00082-4

Deshpande, V.S., Fleck, N.A. (2001). Multi-axial yield behaviour of polymer foams. *Acta Mater.* **49**, 1859-1866. https://doi.org/10.1016/S1359-6454(01)00058-1

Divinycell H: Technical Data (2022): https://www.diabgroup.com/products-services/divinycell-pvc/divinycell-h/

Domander R., Felder A.A., Doube M. (2021). BoneJ2 - refactoring established research software. Wellcome Open Res 2021, **6**:37. https://doi.org/10.12688/wellcomeopenres.16619.2

Dougherty R, Kunzelmann K (2007) Computing local thickness of 3D structures with ImageJ. *Microsc. Microanal.* **13**, 1678-1679. http://doi.org/10.1017/S1431927607074430

Doube, M., Kłosowski, M. et al. (2010). BoneJ: Free and extensible bone image analysis in ImageJ. *Bone* **47**(6), 1076-1079. https://doi.org/10.1016/j.bone.2010.08.023

Drucker, D.C. and Prager, W. (1952). Soil mechanics and plastic analysis for limit design. *Quart. Appl. Math.* **10**, 157-165. https://doi.org/10.1090/qam/48291

Gaitanaros, S., Kyriakides, S. (2014). Dynamic crushing of aluminum foams: Part II – Analysis. *Int. J. Solids Struct.* **51**, 1646–1661. https://doi.org/10.1016/j.ijsolstr.2013.11.020

Gaitanaros, S., Kyriakides, S., Kraynik A.M. (2012). On the crushing response of random open-cell foams. *Int'l J. Solids Struct.* **49,** 2733-2743. http://doi.org/10.1016/j.ijsolstr.2012.03.003

Gibson, L.J., Ashby, M.F., Zhang, J., Triantafillou, T.C. (1989). Failure surfaces for cellular materials under multiaxial loads—I. Modeling. *Int'l J. Mech. Sciences* **31**, 635-663. https://doi.org/10.1016/S0020-7403(89)80001-3

Gibson, L.J., Ashby, M.F. (1997). *Cellular Solids: Structure and Properties, 2nd Ed.* Cambridge University Press. https://doi.org/10.1017/CBO9781139878326

Gibson, L.J., Ashby, M.F., Harley, B.A (2010). *Cellular Materials in Nature and Medicine.* Cambridge University Press.

Gioux, G., McCormack, T.M., Gibson, L.J. (2000). Failure of aluminum foams under multiaxial loads. *Int'l J. Mech. Sci.* **42**, 1097-1117. https://doi.org/10.1016/S0020-7403(99)00043-0

Gong, L., Kyriakides S., Jang, W.-Y. (2005). Compressive response of open-cell foams. Part I: Morphology and elastic properties. *Int'l J. Solids Structures* **42**, 1355-1379. https://doi.org/10.1016/j.ijsolstr.2004.07.023

Greer, J.R. and Deshpande, V.S. (2019). Three-dimensional architected materials and structures: Design, fabrication, and mechanical behavior. *MRS Bulletin* **44**(10), pp.750-757. https://doi.org/10.1557/mrs.2019.232

Jang, W.Y., Hseieh, W.Y., Miao, C.C., Yen, Y.C. (2015). Microstructure and mechanical properties of ALPORAS closed-cell aluminium foam. *Mater. Charact.* **107**, 228-238. https://doi.org/10.1016/j.matchar.2015.07.012

Jang, W.-Y., Kraynik, A.M., Kyriakides, S. (2008). On the microstructure of open-cell foams and its effect on elastic properties. *Int'l J. Solids Struct.* **45**, 1845-1875. https://doi.org/10.1016/j.ijsolstr.2007.10.008

Jang, W.-Y., Kyriakides, S. (2009). On the crushing of aluminum open-cell foams: Part I experiments. *Int'l J. Solids Struct.* **46**, 617-634. https://doi.org/10.1016/j.ijsolstr.2008.09.008

Liu, Y., Rahimidehgolan, F., Altenhof, W. (2020). Anisotropic compressive behavior of rigid PVC foam at strain rates up to 200 s^{-1}. *Polymer Test.* **91**, 106836. https://doi.org/10.1016/j.polymertesting.2020.106836

Pascalis, F.D., Nacucchi, M., Scatto, M., Albertoni, R. (2016). Quantitative characterisation of low-density, high performance polymeric foams using high resolution X-ray computed tomography and laser confocal microscopy. *NDT&E Int* **83,** 123–33. https://doi.org/10.1016/j.ndteint.2016.06.010

Rahimidehgolan, F., Altenhof, W. (2023). Compressive behavior and deformation mechanisms of rigid polymeric foams: A review. *Composites B* **253**, 110513. https://doi.org/10.1016/j.compositesb.2023.110513

Ruan, D., Lu, G., Ong, L.S., Wang, B. (2007). Triaxial compression of aluminum foams. *Comp. Sci. and Tech.* **67**, 1218-1234. https://doi.org/10.1016/j.compscitech.2006.05.005

Salvo, L., Cloetens, P., Maire, E., Zabler, S., Blandin, J.J, Buffiere, J.Y., Ludwig, W., Boller, E., Bellet, D., Josserond, C. X-ray micro-tomography an attractive characterisation technique in materials science. *Nucl. Instrum. Methods Phys. Res. B* **200**, 273–286. https://doi.org/10.1016/S0168-583X(02)01689-0

Schaedler, T.A., Carter, W.B. (2016). Architected cellular materials. *Annual Rev. Mat. Resea.* **46**, 187-210. https:doi.org/10.1146/annurev-matsci-070115-031624

Schindelin, J., Arganda-Carreras, I., et al. (2012). Fiji: an open-source platform for biological-image analysis. *Nature Methods* **9**(7), 676–682. http://doi.org/10.1038/nmeth.2019

Shafiq, M., Ayyagari, R.S., Ehaab, M., Vural, M. (2015). Multiaxial yield surface of transversely isotropic foams: Part II Experimental. *J. Mech. Physics Solids* **76**, 224-236. https://doi.org/10.1016/j.jmps.2014.10.009

Shaw, M.C., Sata, T. (1966). The plastic behavior of cellular materials. *Int'l J. Mech. Sciences* **8**, 469-478. https://doi.org/10.1016/0020-7403(66)90019-1

Su, B.Y., Huang, C.-M., Shang H., Jang, W.Y. (2018). The effect of cell-size dispersity on the mechanical properties of closed-cell aluminum foams. *Mater. Charact.* **135**, 203-213. https://doi.org/10.1016/j.matchar.2017.11.035

Su, B.Y., Jang, W.Y. (2022). The microstructure characterization and elastic properties of closed-cell foams. *Int'l J. Solids Struct*. **257**, 111700. https://doi.org/10.1016/j.ijsolstr.2022.111700

Tang, Y., Zhang, W., Jiang, X., Zhao, J., Xie, W., Chen, T. (2022). Experimental investigations on phenomenological constitutive model of closed-cell PVC foam considering the effects of density, strain rate and anisotropy. *Composites B* **238**, 109885. https://doi.org/10.1016/j.compositesb.2022.109885

Tomin, M., Kmetty, Á. (2022). Polymer foams as advanced energy absorbing materials for sports applications—a review. *J. Appl. Polym. Sci.* **139**, 51714. https://doi.org/10.1002/app.51714

Triantafillou, T.C., Zhang, J., Shercliff, T.L., Gibson, L.J., Ashby, M.F. (1989). Failure surfaces for cellular materials under multiaxial loads - II. Compression of models with experiment. *Int'l J. Mech. Sciences* **31**, 665-678. https://doi.org/10.1016/S0020-7403(89)80002-5

Virtanen, P., Gommers, R., Oliphant, T.E. et al. (2020). SciPy 1.0: fundamental algorithms for scientific computing in Python. *Nat. Methods* **17**, 261–272. https://doi.org/10.1038/s41592-019-0686-2

Yang, C., Kyriakides, S. (2019). Multiaxial crushing of open-cell foams. *Int'l J. Solids Struct*. **159,** 239-256. https://doi.org/10.1016/j.ijsolstr.2018.10.005

Yang, C., Kyriakides, S. (2020a). Continuum modeling of crushing of low density foams. *J. Mech. Phys. Solids* **136,** 103688. https://doi.org/10.1016/j.jmps.2019.103688

Yang, C., Kyriakides, S. (2020b). Crushing of low density foams under triaxial loadings. *Extr. Mech. Let.* **35**, 100620. https://doi.org/10.1016/j.eml.2019.100620

Zheng, Z., Wang, C., Yu, J., Reid, S.R., Harrigan, J.J. (2014). Dynamic stress–strain states for metal foams using a 3D cellular model. *J. Mech. Physics Solids* **72**, 93-114. http://dx.doi.org/10.1016/j.jmps.2014.07.013

Zhu, C., Zheng, Z., Wang, S., Zhao, K., Yu, J. (2019). Modification and verification of the Deshpande–Fleck foam model: A variable ellipticity. *Int'l J. Mech. Sci.* **151**, 331-342 https://doi.org/10.1016/j.ijmecsci.2018.11.028

Zhou, Y., Xue, B., Zhang, W., Wang, R. (2023). Prediction of bulk mechanical properties of PVC foam based on microscopic model: Part I-Microstructure characterization and generation algorithm. *Polym. Test.* **117**, 107872.https://doi.org/10.1016/j.polymertesting.2022.107872

Vita

Joe Skeens was born in Columbus, Ohio. He graduated from Grandview Heights High School in the Columbus suburbs in 2015. He graduated from Purdue University with a Bachelor of Science degree in Aeronautical and Astronautical Engineering in 2019. He enrolled in graduate school at The University of Texas at Austin in 2019 to pursue a Ph.D. in Aerospace Engineering.

Permanent email: joeskeens1@gmail.com

This thesis was typed by the author.